



January 2015

Multi-Doppler Radar And In Situ Cloud Hydrometeor Analysis Of A North Dakota Snowband And Its Environment On 20 November 2010

Kendell Laroche

Follow this and additional works at: <https://commons.und.edu/theses>

Recommended Citation

Laroche, Kendell, "Multi-Doppler Radar And In Situ Cloud Hydrometeor Analysis Of A North Dakota Snowband And Its Environment On 20 November 2010" (2015). *Theses and Dissertations*. 1798.
<https://commons.und.edu/theses/1798>

This Thesis is brought to you for free and open access by the Theses, Dissertations, and Senior Projects at UND Scholarly Commons. It has been accepted for inclusion in Theses and Dissertations by an authorized administrator of UND Scholarly Commons. For more information, please contact zeinebyousif@library.und.edu.

MULTI-DOPPLER RADAR AND IN SITU CLOUD HYDROMETEOR ANALYSIS OF A
NORTH DAKOTA SNOWBAND AND ITS ENVIRONMENT ON 20 NOVEMBER 2010

by

Kendell Thomas LaRoche
Bachelor of Science, Metropolitan State University of Denver, 2011

A Thesis
Submitted to the Graduate Faculty

of the

University of North Dakota

In partial fulfillment of the requirements

for the degree of

Master of Science

Grand Forks, North Dakota


August


2015

c 2015 Kendell LaRoche

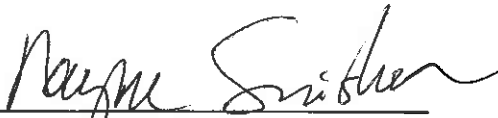
This thesis, submitted by Kendell LaRoche in partial fulfillment of the requirements for the Degree of Master of Science from the University of North Dakota, has been read by the Faculty Advisory Committee under whom the work has been done and is hereby approved.

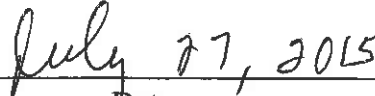

Dr. Matthew Gilmore


Dr. Mark Askelson


Dr. David Delene

This thesis meets the standards for appearance, conforms to the style and format requirements of the Graduate School of the University of North Dakota, and is hereby approved.


Dean of the Graduate School


Date

PERMISSION

Title Multi-Doppler Radar and In Situ Cloud Hydrometeor Analysis of A North Dakota Snowband and its Environment on 20 November 2010

Department Atmospheric Science

Degree Master of Science

In presenting this thesis in partial fulfillment of the requirements for a graduate degree from the University of North Dakota, I agree that the library of the University shall make it freely available for inspection. I further agree that permission for extensive copying for the scholarly purposes may be granted by the professor who supervised my thesis work or, in his absence, by the Chairperson of the department or the dean of the School of Graduate Studies. It is understood that any copying or publication or other use of this thesis or part thereof for financial gain shall not be allowed without my written permission. It is also understood that due recognition shall be given to me and to the University of North Dakota in any scholarly use which may be made of any material in my thesis.

Kendell LaRoche

July 21, 2015

TABLE OF CONTENTS

LIST OF FIGURES.....	vii
LIST OF TABLES.....	ix
ACKNOWLEDGEMENTS.....	x
ABSTRACT.....	xi
CHAPTER	
I. INTRODUCTION.....	1
Snowbands.....	1
General Definition of a Snowband.....	2
Doppler Radar Velocity Measurements.....	3
Dual-Polarization Parameters.....	3
Dual-Polarization Parameter Values Associated with Snowbands.....	6
Snowband Formation.....	10
Snowband Microphysics and Structural Characteristics.....	10
Thesis.....	14
II. DATA AND METHODOLOGIES.....	16
Equipment.....	16
Data Processing.....	18
Radar Data Quality Assurance.....	18
Radar Format Conversion and Objective Analysis.....	21

	Artifacts Arising from Multi-Doppler Objective Analysis Process.....	22
	Multi-Doppler Wind Retrieval.....	24
	Multi-Doppler Velocity Retrievals.....	26
	Aircraft Data Analysis.....	27
	Radar Imaging Software.....	28
	Radar-Aircraft Transect Analysis.....	28
III.	RESULTS.....	30
	Aircraft Results.....	31
	Radar Results.....	41
	First Transect-pair: 2.71 km AGL.....	44
	Second Transect-pair: 2.41 km AGL.....	49
	Third Transect-pair: 1.80 km AGL.....	52
	Fourth Transect-pair: 1.19 km AGL.....	56
	Fifth Transect-pair: 0.89 km AGL.....	60
	Radar-Aircraft Transect Analysis Results.....	64
	Aircraft and Radar Analysis Through Snowband Core and Edge.....	67
IV.	DISCUSSION.....	69
	Summary of Results.....	69
	Comparisons with Previous Literature.....	71
	Project Limitations.....	74
V.	CONCLUSIONS.....	77
	APPENDICES.....	82
	REFERENCES CITED.....	86

LIST OF FIGURES

Figure	Page
1. Vertical cross sections through a snowband on 18 January 1992.	11
2. UND and DOW radial velocity plot with marked location of 0 m s^{-1} contour.	20
3. Radial velocity plots from DOW radar before (a) and after (b) data removal.	21
4. CAPPI images of w at 3.0 km from dual-Doppler analysis showing (a) anomalous circles and (b) w after additional smoothing was applied to remove these circles.	24
5. Cloud particle concentration versus diameter (a), two-dimensional cloud particle images taken inside (b), and outside (c) the snowband at 2.71 km.	36
6. Same as Figure 5, except at 2.41 km.	37
7. Same as Figure 5, except at 1.80 km.	38
8. Same as Figure 5, except at 1.19 km.	39
9. Same as Figure 5, except at 0.89 km.	40
10. CAPPI plot of retrieved vertical velocity at 0.5 km with horizontal wind vectors.	42
11. Aircraft transects inside and outside of the snowband overlaid with DOW reflectivity at (a) 2.75 km, (b) 2.50 km, (c) 1.75 km, (d) 1.25 km, and (e) 1.00 km.	44
12. Plots of vertical velocity at 2.75 km AGL overlaid with the locations of the Citation Research Aircraft flight transects inside (a) and outside the snowband (b).	46
13. Plots of vertical velocity overlaid with contours of reflectivity along the aircraft transect in (a) and outside of (b) the snowband for the first transect-pair.	47
14. Radar reflectivity cross sections along the aircraft transect inside (a) and outside (b) the snowband for the first transect-pair.	47
15. Radar reflectivity slices with wind vectors at 2.75 km AGL.	48

16. Plots of vertical velocity at 2.5 km AGL overlaid with the locations of the Citation Research Aircraft flight transects inside (a) and outside the snowband (b).	50
17. Plots of vertical velocity overlaid with contours of reflectivity along the aircraft transect in (a) and outside of (b) the snowband for the second transect-pair.	51
18. Radar reflectivity cross sections along the aircraft transect inside (a) and outside (b) the snowband for the second transect-pair.	51
19. Plots of vertical velocity at 1.75 km AGL overlaid with the locations of the Citation Research Aircraft flight transects inside (a) and outside the snowband (b).	54
20. Plots of vertical velocity overlaid with contours of reflectivity along the aircraft transect in (a) and outside of (b) the snowband for the third transect-pair.	55
21. Radar reflectivity cross sections along the aircraft transect inside (a) and outside (b) the snowband for the third transect-pair.	55
22. Radar reflectivity slices with wind vectors at 1.75 km AGL.	56
23. Plots of vertical velocity at 1.25 km AGL overlaid with the locations of the Citation Research Aircraft flight transects inside (a) and outside the snowband (b).	58
24. Plots of vertical velocity overlaid with contours of reflectivity along the aircraft transect in (a) and outside of (b) the snowband for the fourth transect-pair.	59
25. Radar reflectivity cross sections along the aircraft transect inside (a) and outside (b) the snowband for the fourth transect-pair.	59
26. Radar reflectivity slices with wind vectors at 1.25 km AGL.	60
27. Plots of vertical velocity at 1.0 km AGL overlaid with the locations of the Citation Research Aircraft flight transects inside (a) and outside the snowband (b).	62
28. Plots of vertical velocity overlaid with contours of reflectivity along the aircraft transect in (a) and outside of (b) the snowband for the fifth transect-pair.	63
29. Radar reflectivity cross sections along the aircraft transect inside (a) and outside (b) the snowband for the fifth transect-pair.	63
30. Reflectivity and dual-polarization trends for both radars along the time-to-space corrected Citation Research Aircraft transects both inside and outside the snowband.	66
31. Geometry diagrams used to compute diameter of hydrometeors sampled by 2DC probe.	84

LIST OF TABLES

Table	Page
1. Definition and characteristics of different types of radar-observed precipitation bands.	2
2. Polarimetric radar threshold values observed for different hydrometeor species.	9
3. Polarimetric radar values of ice crystals observed by airborne cloud radar.	9
4. Polarimetric radar threshold values for classifying snow-crystals.	9
5. Polarimetric radar threshold values for classifying hydrometeor species.	10
6. Specifications of the different radars used in this study.	16
7. Default and chosen radius of influence values used in Reorder.	24
8. Reflectivity values used to distinguish if the aircraft was in the snowband core, along the snowband edge, or outside the snowband.	31
9. Measurements from various transects completed using the Citation Research Aircraft.	35
10. Average values of Z , Z_{DR} , K_{DP} , and ρ_{HV} along each transect made by the Citation Research Aircraft both inside and outside the snowband for the DOW radar, in addition to the column average.	67
11. Same as Table 10, except for UND radar.	67
12. Average reflectivity and Z_{DR} from transect through the snowband core and edge at 2.71km.	68
13. Same as Table 12, except at for transect at 0.89 km.	68

ACKNOWLEDGEMENTS

I would like to thank all my advisors, Dr. Matthew Gilmore, Dr. Mark Askelson, and Dr. David Delene for their excellent guidance, helpful support, and expertise when assisting with my thesis. I would also like to thank Christopher Theisen for his radar data expertise, both and Michael Poellot and Andrea Neumann for their knowledge of the aircraft instruments and data, and Holly Robak for her previous research on this topic.

I would also like to extend my thanks to all the faculty, staff, and fellow graduate students in the Department of Atmospheric Sciences for their contribution, no matter how small. Finally I would like to thank my family for their unending support through this long process.

ABSTRACT

Snowbands can produce locally larger snowfall accumulations as well as reductions in visibility thereby being hazardous to vehicles and aircraft. The study herein is the first to combine multi-Doppler retrieved winds, *in situ* snow crystal size distributions, and polarimetric radar variables within snowbands for two radar wavelengths. Data includes two polarimetric radars: Doppler on Wheels (DOW) – a mobile X-band polarimetric Doppler weather radar – and the University of North Dakota (UND) polarimetric C-band radar (hereafter: “UND radar”). Also used in this study are data from the two-dimensional cloud (2DC) probe attached to the UND’s Citation II weather research aircraft. Retrieved wind velocities, from dual-Doppler analysis, and dual polarization radar variables, are matched to the aircraft’s transect location and 2DC probe images inside and outside the snowband.

Regarding kinematics, upward motion in both the retrieved vertical wind and aircraft-measured winds is seen generally west of the DOW location with downward motion generally east. The dual-Doppler retrieved horizontal winds also show easterly flow at lower altitudes and westerly at higher altitudes, consistent with a sounding from Bismarck, ND. These wind patterns are generally persistent in the local environment regardless of the snowband’s presence.

Ice hydrometeors, measured by the 2DC probe, are more numerous and larger inside the snowband, compared to a weaker-reflectivity snow-filled region outside the snowband. These differences in number concentrations are present at all altitudes sampled but are most distinct at higher altitudes. Along the aircraft transects, both radars observe larger average K_{DP} values (most altitudes) and larger average ρ_{HV} values (all altitudes) inside the snowband.

Differences exist between the same radar variable for near-simultaneous dual radar measurements. These differences are: greater reflectivity (regardless of altitude and location) for DOW compared to UND, greater average ρ_{HV} for the DOW radar compared to UND, closer-to-0 dB average Z_{DR} values for DOW inside the snowband, and closer-to-0 dB average Z_{DR} values for UND outside the snowband. These radar variable differences could be related to calibration and wavelength differences between the DOW and UND, slight differences in the sampling area, and small scale variability within the snowband.

Radar reflectivity (greater values inside the snowband) and Z_{DR} (values closer to 0 dB inside the snowband) are consistent with the original hypothesis. However vertical velocity has similar values both inside and outside the snowband. Stronger radar reflectivity and Z_{DR} closer to 0 dB do not coincide with stronger updrafts inside the snowband.

This snowband had unique polarimetric and hydrometeor size distribution characteristics compared to its surroundings. The characteristics inside and outside the snowbands determined from this study, could be used to improve the microphysical parameterization within forecasting models of cold season events. Better microphysical parameterization could improve the forecasted timing, duration, and snowfall amounts from snowbands, improving transportation safety and efficiency. Also, because retrieved vertical velocity does not differ significantly inside versus outside the snowband, another process is

responsible for larger aggregate hydrometeors within the snowband. Another atmospheric process, such as slantwise convection, could be the reason the snowbands in the study formed.

To improve upon this study, more information on the precipitation size hydrometeor characteristics is needed, in addition to surface conditions both inside and outside snowbands. To make these critical observations, future field experiments should include the following aircraft and surface-based instruments. Adding measurements from a High Volume Precipitation Spectrometer probe, the full size spectrum of precipitation-size hydrometeors could be sampled. Surface snowfall and visibility measurements both inside and outside the snowband could be used to better quantify snowband impacts at and near ground level.

CHAPTER I

INTRODUCTION

Snowbands

Snowbands can produce higher snow accumulations (Kocin and Uccellini 2004) which can lead to reduced visibility for vehicles and aircraft, and prove challenging when it comes to forecasting snowband intensity and location (Novak and Colle 2012). Knowing that snowbands can occur in the northwest quadrant of extratropical cyclones (Cronce et al. 2007; Novak et al. 2009) can be helpful in prediction their general location. The National Weather Service Doppler Radar (WSR-88D) network can be used in the detection and monitoring of these small-scale hazardous weather events. Now that the WSR-88D network has been upgraded to Polarimetric, which has the capability to remotely infer precipitation type and phase (Zrnić and Ryzhkov 1999; Straka et al. 2000; Zrnić et al. 2001), improved snowband detection and monitoring holds promise. However, gaps in our current understanding of snowband microphysics still exist. How do polarimetric radar observations compare to the crystals observed *in situ* within snowbands? What do the airflow patterns within snowband reveal about their microphysical properties? Improved understanding of snowbands could lead to better short-term forecasts and improve transportation safety and efficiency.

General Definition of a Snowband

Banded structure is defined as the arrangement of radar precipitation echoes in the form of long lines or bands (Glickman 2000, p. 72) with larger radar reflectivity inside the snowband. Banded structures may contain both liquid and solid precipitation, and occur with various longevity, size, and intensity (Table 1). If temperatures measured at the surface and aloft are much colder than the melting temperature, the banded structures may be referred to as snowbands.

Table 1. Definition and characteristics of different types of radar-observed precipitation bands. Adapted from Novak et al. (2004).

Band Definition	Band Characteristics		
	Intensity	Size	Time
Single band	Min of 30 dBZ along majority of band length	20-100 km width, greater than 250 km length	At least 2 hours
Multi band	More than three bands with similar spacing and orientation, reflectivities greater than 10 dBZ over the surrounding reflectivity, spacing between bands no greater than 40 km	Each band 5 – 20 km wide	At least 2 hours
Narrow cold-front band	Min of 40 dBZ, usually found along the surface cold front or within the cyclone warm sector	10 – 50 km width, greater than 300 km length	At least 2 hours
Transitory banded structure	Band structure meets all necessary criteria for a category except one		

Radar reflectivity values are larger in snowbands because the hydrometeors there are more numerous and/or greater in size than hydrometeors outside the snowband. Larger hydrometeors backscatter more power, as can be seen in the relation between logarithmic radar reflectivity factor and hydrometeor size and number

$$Z = \sum_{i=1}^n N_i D_i^6, \quad (1)$$

where Z is the linear radar reflectivity factor ($\text{mm}^6 \text{ m}^{-3}$) and N_i is the number of drops of diameter D_i (Rinehart 2010, p. 94-95). One possible reason for larger hydrometeors in snowbands is snow crystals that stick together as they fall due to the aggregation process. These clusters of snow crystals are called aggregates (Glickman 2000, p. 20).

Doppler Radar Velocity Measurements

A Doppler radar has the ability to measure the component of velocity of a target along the radial direction (direction in which the radar is pointing). The measured velocity is relative to the radar and not the target's actual velocity, unless the target is moving directly towards or away from the radar. A target's radial velocity can be obtained from the frequency shift which can be measured by

$$f_{shift} = \frac{2V_{radial}}{\lambda} \quad (2)$$

where f_{shift} is the frequency shift (m s^{-1}), V_{radial} is the component of the target's velocity (m s^{-1}) along the radial, and λ is the radar wavelength (m) (Rinehart 2010, p. 97-100). Recall from vector calculus, that the projection of the target's velocity onto the along-beam direction is $V_{radial} = V \cos(\alpha)$, where α is the angle the target is moving relative to the radar pointing direction.

Dual-Polarization Parameters

Within recent years dual-polarization has been implemented across the entire WSR-88D network and enables hydrometeor characteristics to be determined. Dual-polarization techniques have the ability to detect different hydrometeor types within clouds using horizontal and vertical polarized electric fields (Rinehart 2010, p. 432). The three dual-

polarization parameters used in this study are differential reflectivity (Z_{DR}), specific differential phase (K_{DP}), and correlation coefficient (ρ_{HV}). These radar parameter mathematical definitions and physical interpretations follow below.

The equation for Z_{DR} (dB) is

$$Z_{DR} = 10 \log_{10} \left(\frac{Z_h}{Z_v} \right), \quad (3)$$

where Z_h and Z_v are the linear radar reflectivity ($\text{mm}^6 \text{m}^{-3}$) along the horizontal and vertical polarizations, respectively (e.g., Rinehart 2010, p. 420). Positive values of Z_{DR} (dB) indicate that the dominant (largest) hydrometeors in the volume are longer along the horizontally-polarized beam, on average. Negative values of Z_{DR} indicate that the dominant hydrometeors in the volume are longer along the vertically-polarized beam, on average. Differential reflectivity values of zero indicate that the dominant particles do not have, on average, a preferred orientation axis, or that the particles are spherical. For small elevation angles, the horizontally-polarized beam is roughly parallel to the ground along the long axis of a raindrop and thus would give positive Z_{DR} values. For a 90° elevation angle (radar pointed straight up), those same raindrops would have negative Z_{DR} values.

Propagation differential phase (ϕ_{dp}) is the phase difference for horizontally and vertically polarized waves (Rinehart 2010, p. 420). For small elevation angles, positive differential propagation phase shifts indicate that there are oblate (wider than they are tall) scatterers such as large raindrops (Kennedy and Rutledge 2011). The phase shift is related to the size, shape, orientation, and index of refraction of the hydrometeor. However, because ϕ_{dp} is additive along the radar beam, it is difficult to interpret. Instead, by taking the derivative of ϕ_{dp} along the radial, one may identify the location along the radial where the

greatest phase shifts are occurring, which makes K_{DP} physically related to rain rate. K_{DP} is given by

$$K_{DP} = \frac{\varphi_{DP}(r_2) - \varphi_{DP}(r_1)}{2(r_2 - r_1)}, \quad (4)$$

where K_{DP} is measured in units of $^{\circ} \text{ km}^{-1}$, φ_{dp} is the two-way propagation differential phase (degrees), and r is range (km) (e.g., Rinehart 2010, p. 214). Larger raindrops are more oblate and cause greater differences in attenuation and phase shift between the two polarized waves, resulting in larger K_{DP} values.

For shallow elevation angles, positive (negative) values mean the hydrometeors are wider (taller) than they are tall (wide), and 0 means randomly oriented hydrometeors (Rinehart 2010, p. 214). K_{DP} is primarily used to detect different hydrometeor species. Positive values of K_{DP} indicate large raindrops ($> 0.6 ^{\circ} \text{ km}^{-1}$), which are wider than they are tall, values of 0 indicate falling hail or very small water drops (0 to $1 ^{\circ} \text{ km}^{-1}$), and negative values of K_{DP} indicate graupel (-0.5 to $1.5 ^{\circ} \text{ km}^{-1}$) (Straka et al. 2000). Measurements of K_{DP} are dominated by oblate raindrops and not very affected by the presence of hail, as long as the hail appears symmetric to the radar. K_{DP} is a useful for estimating rainrate in mixtures of rain and hail (Aydin et al. 1995).

Correlation coefficient ($\rho_{HV}(0)$) is the correlation between the vertically and horizontally polarized signals at a point in space at the same time (“(0)”). Co-polar correlation coefficient (ρ_{HV}) varies between 0 and 1 and is given by (Brandes, 2000)

$$\rho_{HV} = \frac{\langle s_{VV} s_{HH}^* \rangle}{\langle |s_{HH}|^2 \rangle^{1/2} \langle |s_{VV}|^2 \rangle^{1/2}}, \quad (5)$$

where s and s^* are scattering matrices, and H and V subscripts represent the transmitted and received polarizations for horizontal and vertical signals. Different hydrometeors are

associated with different ρ_{HV} magnitudes. Perfect spheres give ρ_{HV} of 1.0 whereas, rain is usually between 0.97 – 0.99 depending on intensity. Hydrometeors with irregular shapes, including snow, are less than 0.95 (Rinehart 2010, pp. 215 – 216). Much smaller values can indicate non-meteorological signals such as birds, (Rinehart 2010, p. 217) and tornado debris (Ryzhkov et al. 2005).

Polarimetric measurements have the potential to remotely determine the melting or freezing layer because of the polarimetric measurements sensitivity to the large, wetted particles that occur in the melting layer (Ikeda and Brandes 2003). The height of the melting layer is very important in determining what type of precipitation will eventually reach the ground. Changes in melting layer height over time will change the type of precipitation that could reach the ground (Scharfenberg and Maxwell 2003). If the precipitation reaching the ground is liquid, K_{DP} intensity is closely related to rainfall intensity, and can be used for quantitative rainfall estimation (Wang and Chandrasekar 2009).

Dual-Polarization Parameter Values Associated with Snowbands

While using a mobile X-band radar to examine relationships between dual-polarization observations and long-lake axis parallel lake-effect snowbands over Lake Ontario, Cermak et al. (2012) found that larger Z_{DR} values were observed in convective cells near the snowband rather than in the primary snowband itself. Larger Z_{DR} values in nearby convective cells were present even though reflectivity values for both the snowband and convective cells were similar for that particular case. Another case had similar Z_{DR} values between snowbands and nearby convective cells. The Z_{DR} value differences for each case were likely related to differences in ice crystal orientation relative to each case location. Values of K_{DP} were also examined by Cermak et al., and were similar for convective cells

and snowbands. Ahasic et al. (2012) compared values of Z , Z_{DR} , K_{DP} , and ρ_{HV} from an X-band radar to ground-observed hydrometeor type at two locations during four lake-effect snow events. During these events snow pellets, dendrites, and a mix of pellets and dendrites were recorded. Dendrites had the highest mean Z (24.3 dBZ), the lowest mean Z_{DR} (0.3), the highest mean K_{DP} ($-0.11 \text{ } ^\circ \text{ km}^{-1}$), and the highest mean ρ_{HV} (0.981). Mean Z_{DR} values for pellets were higher (0.66 dB) than dendrites, with the authors concluding that a relationship was evident between Z_{DR} and hydrometeor type.

Using a measurements from the 10-cm-wavelength Cimarron polarimetric weather radar in Oklahoma, Ryzhkov and Zrnich (1998) obtained measurements that show that snow storms that produce aggregates generally have higher reflectivity values with lower Z_{DR} and K_{DP} values than those with an abundance of small ice crystals. Average Z_{DR} values for snowstorms in Oklahoma with an abundance of small ice crystals and no aggregates ranged between 0.3 to 0.6 dB while the average Z_{DR} values in snowstorms containing aggregates were between 0.2 to 0.5 dB. Average K_{DP} values in snowstorms containing aggregates ranged between 0.01 and $0.06 \text{ } ^\circ \text{ km}^{-1}$ while the average values in snowstorms that did not contain aggregates were between 0.04 and $0.75 \text{ } ^\circ \text{ km}^{-1}$. The larger snowflakes and aggregates are more likely to tumble as they fall. This tumbling would decrease values of Z_{DR} and K_{DP} and make areas of aggregates distinguishable from small ice crystals.

Measurements from *in situ* aircraft are also consistent with radar data. Meischner et al. (1991) used aircraft data collected through the melting layer of a moderately precipitating stratiform system along with dual-polarization C-band radar to determine hydrometeor characteristics. Data from Meischner et al. showed that aggregates had higher reflectivity and Z_{DR} values generally close to 0 dB. However large aggregates with low density had high

reflectivity but large Z_{DR} values, indicating that the large aggregates were oriented horizontally. Samples of needles had low reflectivity and positive values for Z_{DR} . Graupel and drops in the melting layer had high reflectivity and positive Z_{DR} values; while drops below the melting layer had reflectivity lower than those inside the melting layer and Z_{DR} values around 0 dB. A time series analysis constructed from a range-height indicator (RHI) scan had a section with high values for reflectivity and Z_{DR} , which the authors concluded contained aggregates or wet, melting snowflakes (Table 2). Wolde and Vali (2001) used an airborne 95 – GHz (3 mm wavelength) polarimetric cloud radar to sample different cloud types. From their results planar crystals produced the highest Z_{DR} values for near-horizontal radar beam angles, between 4 to 9 dB. Dendritic crystals had lower Z_{DR} values of $\sim 0.5 - 3.5$, and columnar crystals were between 2 – 4 dB (Table 3).

Finally previous studies have constructed thresholds for different radar parameters for snow crystals based on hydrometeor classification and modeling studies. Straka et al. (2000) constructed a table of threshold values for snow crystal and aggregate radar values based on observational measurements with 10-cm and less wavelength radar and model results (Table 4). May and Keenan (2005) constructed a table of polarimetric variables from a C-band radar along with temperature values in Celsius for different snow crystal types (Table 5). Generally for these studies, wet aggregates had an upper threshold reflectivity of 45 dBZ, larger than dry aggregates and dry crystals. Snow aggregates and dendrites had Z_{DR} values close to 0 dB while most of the dry crystals and wet snow generally had more positive Z_{DR} values. Values of K_{DP} for aggregates were generally lower than K_{DP} values for dry and wet snow. Wet snow had a lower correlation coefficient than dry snow.

Table 2. Polarimetric radar threshold values observed for different hydrometeor species. Adapted from Meischner et al. (1991).

Hydrometeor Species		Z_h (dBZ)	Z_{dr} (dB)
Aggregates		~18	-0.1
	Small	~22	1.2
	Larger, less dense	~24	2.6
Graupel		~18	1.3
Needles		~6	1.6
Drops	Melting region	~18	3.2
	Below melting region	~16	-0.6

Table 3. Polarimetric radar values of ice crystals observed by airborne cloud radar. Observations are at near-horizontal radar beam angles. Arrow indicates increasing values. Adapted from Wolde and Vali (2001).

Crystal Type	Z_h (dBZ)	Z_{dr} (dB)
Unrimed hexagonal plates and stellar crystals		5 – 7
Rimmed plate and branched crystals	4 – 5	0 – 2
Dendritic crystals, unrimed to lightly rimed	~20 ↓	0 ± 0.5
Dendritic crystals, moderately rimed	↓	1.8 ± 0.5
Dendritic crystals, densely rimed	0	1 ± 0.25
Columnar crystals		2 ± 0.5

Table 4. Polarimetric radar threshold values for classifying snow-crystals. Adapted from Straka et al. (2000).

Snow-crystals			Z_h (dBZ)	Z_{dr} (dB)	K_{dp} ($^{\circ}$ km $^{-1}$)	ρ_{HV}	
Snow Aggregate	Dry		< 35	0-1	0-0.2	> 0.95	
	Wet		< 45	0.5-3	0-0.5	0.5 – 0.9	
Dry Crystals	Vertical		< 35	-0.5 to 0.5	-0.6 to 0	> 0.95	
	Horizontal		< 35	0-6	0-0.6	> 0.95	
	Habit	Plate - dendrite		< 35	2-6	0-0.6	> 0.95
		Column - thick plate		< 35	1-4	0-0.6	> 0.95
Needle - sheath			< 35	0-3	0-0.6	> 0.95	

Table 5. Polarimetric radar threshold values for classifying hydrometeor species. Adapted from May and Keenan (2005).

Hydrometeor Species	Z_h (dBZ)	Z_{dr} (dB)	K_{dp} ($^{\circ}$ km$^{-1}$)	ρ_{HV}
Dry snow, low density	-10 to 35	-0.5 to 0.5	-1 to 1	> 0.95
Dry snow, high density (rimed and aggregated)	-10 to 35	0 – 1	0 – 0.4	> 0.95
Wet, melting snow	20 – 45	0.5 – 3	0 – 1	0.5 – 0.9

Snowband Formation

There are several processes that by themselves, or through a combination, can cause snowbands to form. These processes include cold-air damming, local topographic forcing, diabatic processes, cold fronts (Rasmussen et al. 1993), inverted pressure troughs (Kocin and Uccellini 2004), boundary layer instabilities, ducted gravity waves, Kelvin-Helmholtz (K-H) instability, and moist slantwise convection due to the release of conditional symmetric instability (Schultz and Schumacher 1999).

Snowband Microphysics and Structural Characteristics

Previous literature has shown a link between updrafts and ice hydrometeor growth in snowbands. Updrafts enhance the hydrometeor growth process which increases the hydrometeor size and radar reflectivity. Cross section analysis of 2 km tall snowbands in Ishikari Bay, Japan (Kawashima and Fujiyoshi 2005) show low-level wind convergence below 1.0 km when examining radar reflectivity and relative wind vectors normal to the shear-line. As shown in Fig. 1, the converging wind rose to create an updraft with the strongest reflectivity values near the center of the indicated updraft. The wind vectors then begin diverge near the top of the system.

However finds by Steiger et al. (2013) showed asymmetrical RHI structures were identified in 2 – 3 km tall long-lake-axis-parallel snowbands over the Great Lakes. The largest reflectivity values with the greatest vertical extent were displaced either north or south of the strongest updraft region, and low-level convergence and the greatest reflectivity values and were typically not in the snowband geometric center.

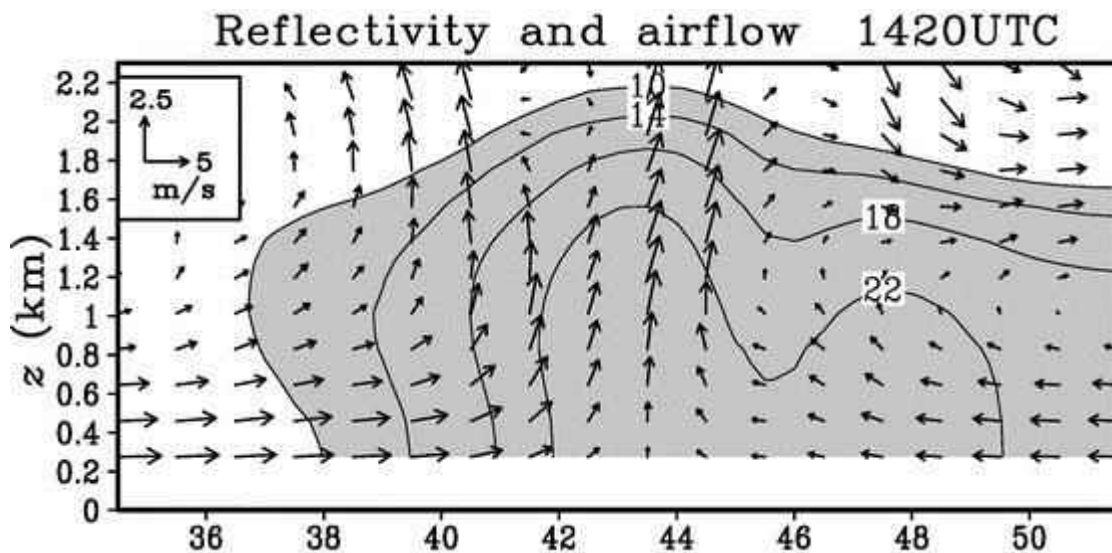


Fig. 1. Mean vertical cross sections through a shear line at 1420 UTC on 18 January 1992. Radar reflectivity (shading and contours) and shear-line-relative wind vectors are shown. Radar reflectivity values greater than 10 dBZ are shaded. Adapted from Kawashima and Fujiyoshi (2005).

The growth characteristics of snow inside a snowband appear to be influenced by the vertical motion. Counce et al. (2007) used a mobile wind profiler to examine updraft velocities and precipitation intensity within bands located in the wraparound quadrant of winter cyclones. The derived measurements from Counce et al. for vertical air motions ranged from -4.3 to $6.7 \text{ m s}^{-1} \pm 0.6 \text{ m s}^{-1}$. The profiler used the signal-to-noise ratio (SNR) to determine precipitation intensity. Regions of upward motion had positive SNR values while regions of downward motion had negative SNR. With system noise approximately constant, Counce et al. found larger, and hence greater precipitation intensity, SNR values within band

updrafts (SNR 5 to 15 dB) compared to band downdrafts (SNR -5 to -15 dB). These results suggest that the updraft portion of snowbands have faster snow growth and larger ice crystals.

Houser and Bluestein (2011) found that K-H waves would produce vertical motions that would transport horizontal momentum vertically, and affect reflectivity and Z_{DR} by mixing different types of crystals and changing the hydrometeor microphysics. Areas of enhanced reflectivity and Z_{DR} were located near areas of upward motion and possibly resulted from ice crystal generation. Their findings determined that K-H waves have the ability to modify precipitation microphysics.

Simultaneous polarimetric radar and aircraft measurements were obtained by Hogan et al. (2002) inside embedded convection in a warm-frontal mixed-phase cloud. The embedded convection appeared to be triggered by K-H instability. Regions of high reflectivity in narrow upright ‘turrets’ also contained regions of Z_{DR} equal to 0 dB. Through the top of one of the turrets, the temperature was -9.4°C , and the vertical velocity was 1.9 m s^{-1} . Concentration of particles larger than $150\text{ }\mu\text{m}$ reached 50 l^{-1} and images of the particles depicted quasi-spherical ice pellets. The authors concluded that lower in the turrets, large graupel and riming snowflakes occurred.

Hydrometeor sizes and concentrations were different inside a snowband than outside a snowband for one case analyzed by Robak et al. (2012) during the Students Nowcasting and Observations with the DOW at UND: Education through Research (SNOWDUNDER) field project in November 2010. Using measurements from an aircraft-mounted cloud imager along with multiple weather research radars, larger hydrometeors with Z_{DR} values of 0 dB were measured inside a snowband. Aircraft cloud probe measurements showed a

greater concentration of smaller particles outside the band and a greater concentration of larger particles inside the band. Although Robak et al. did not analyze the crystal type; Z_{DR} values of 0 dB are consistent with aggregates using a 10-cm wavelength radar (Brandes et al. 1995). This, combined with Ryzhkov and Zrníc (1998) and Meischner et al. (1991), provides evidence that aggregates generally have lower Z_{DR} values (values closer to 0 dB) than pure ice crystals.

Previous work by Plummer et al. (2014 and 2015) analyzed the microphysical structure of stratiform precipitation in the comma head of multiple continental cyclones, an area where snowbands can occur (Cronce et al. 2007; Novak et al. 2009). First Plummer et al. (2014) found a higher concentration of larger hydrometeors and higher values of liquid water content inside generating cells. From the AMS definition: a generating cell is a small region of locally high reflectivity from which a trail of hydrometeors originates (Glickman 2000, p. 332). From Plummer et al. (2014) generating cells were located at or near the cloud top, and from their results larger hydrometeors and higher liquid water content (LWC) were present inside generating cells. Supercooled liquid water (SLW) was also present within the sampled generating cells at temperatures $\geq -31.4^{\circ}\text{C}$. Since SLW is very important for the hydrometeor growth process (Raubert and Tokay 1991), the authors concluded that it was likely that areas of high SLW were favorable locations for ice growth, which were at the top of the cloud.

Plummer et al. (2015) focuses on the fall streaks of hydrometeors produced by cloud-top convective generating cells. Fall streaks were defined as plumes of hydrometeors emanating from convective generating cells. It was found that increased hydrometeor sizes and concentrations produced the observed fall streaks, deposition was an important growth

mechanism below the generating cell level, aggregation became more important with increasing temperature, vertical velocity differences were not significant between fall streaks and the surrounding region, and overall differences in microphysical characteristics were usually observed between temperature intervals. While evidence of enhanced hydrometeor growth was recorded in the fall streaks as oppose to the surrounding area, cloud depth seemed to be more important in the ice growth process. However the majority of grown typically occurred below the generating cell level.

Thesis

From work done by Ryzhkov and Zrnich (1998), Meischner et al. (1991), Straka et al. (2000), Wolde and Vali (2001), and May and Keenan (2005) (**Dual-Polarization Parameter Values Associated with Snowbands**) dual-polarization has the capability to distinguish aggregates from other ice crystal species. Snowband structure documented by Kawashima and Fujiyoshi (2005) and Robak et al. (2012) suggests larger concentrations of large-sized aggregates, with rounder shapes, are expected inside snowbands as compared to their surroundings (**Snowband Microphysics and Structural Characteristics**). However previous work has not combined multi-Doppler measurements with *in situ* aircraft measurements to gain a more in depth understanding of snowbands. Utilizing velocity measurements from multiple weather radars, the three-dimensional flow patterns of snowbands from the SNOWDUNDER data may be retrieved. Over a sample area, polarimetric radar measurements are used to infer hydrometeor type, and *in situ* aircraft measurements are used for verification. Stronger reflectivity and Z_{DR} values closer to 0 dB inside the snowbands should coincide with stronger updrafts within the snowband. This hypothesis is tested for a number of aircraft transects through a single snowband at different

times and altitudes. Consistent behavior amongst many cases, will improve the understanding of snowband kinematics and microphysics.

CHAPTER II
DATA AND METHODOLOGIES

Equipment

Data from two weather radars and the University of North Dakota Cessna Citation II Research Aircraft (herein aircraft) are used. The weather radars include a mobile X-band Doppler radar (DOW) (Center for Severe Weather Research, 2015), and the University of North Dakota NorthPOL C-band radar (University of North Dakota, 2015) (herein UND) (Table 6).

Table 6. Specifications of the different radars used in this study.

Radar	DOW 6	UND
Antenna Diameter (m)	2.44	3.66
Beamwidth (°)	0.93	0.99
Frequency (GHz)	9.40	5.55
Band	X	C
Peak Power (kW)	500	250
PRF (Hz)	1000	1000
Nyquist velocity (m s^{-1})	7.8	13.4
Dual Polarization during experiment	Yes	Yes

The device used to measure hydrometeors is a two-dimensional cloud (2DC) probe from Particle Measuring Systems, Inc, and is attached to the wing of the aircraft. The 2DC provides measurements of the size distributions and concentration of cloud hydrometeors. Hydrometeor two-dimensional information is obtained by creating successive image slices of hydrometeor shadows as hydrometeors pass through a single linear photodiode array

sampling volume containing 32 diodes, each 30 μm in size. This instrument can measure hydrometeors from 15 – 45 μm to approximately 3000 μm . However due to instrument noise the first few particle bins are sometimes removed. A laser is shined onto the diodes which the diodes register as ‘on’ and given a bit value of 0. When a particle passes through the laser the particle shadow blocks the laser from reaching a number of these diodes. Diodes that register a 50% reduction in light intensity are shadowed, and have a diode bit set to 1 as oppose to 0 when a particle shadow is not registered. Data from the 2DC probe is asynchronous which means data is only recorded when hydrometeors are present. Collected data is usually in 1 Hz intervals unless otherwise specified (Particle Measuring Systems, Inc. 2015).

For accurate samples, the aircraft must be flying at an airspeed that will move the probe ahead 30 μm to maintain the same size resolution. If the aircraft is flying too fast or too slow, the image slice resolution would not match the size of the diode, creating skewed hydrometeor images. Aircraft speed is sent to probe every one second and is used to adjust the sampling frequency of the diodes to maintain equally sized slice resolution. The number of hydrometeors sampled over a given time interval is determined by the total length of all the diodes, the laser width, the speed of the aircraft, and the length of time between timing bars. Hydrometeor size is then calculated for each sampled hydrometeor using a particle reconstruction method (Heymsfield and Parrish 1978). For information on the process used to reconstruction sampled hydrometeors, see Appendix A.

Three dimensional wind vectors are estimated from the difference between the aircraft ground and air speeds. The air speed is determined from five pressure ports located on the nose of the Citation Research Aircraft. These ports are connected by tubes to a

pressure transducer located inside the aircraft nose. Aircraft ground speed measurements are obtained using the Applanix Position and Orientation System (POS). This system consists of an Inertial Measurement Unit, GPS antenna, and POS computer system. An optimally accurate navigation solution is computed from the POS system computer using both the inertial and GPS information (Delene 2015). The equations for solving for the three dimensional wind vectors are provided by Lenschow (1986).

Data Processing

Radar Data Quality Assurance

Quality assurance is conducted on the raw radar data to remove ground clutter and correct aliased radial velocity data. Radar data are then placed on to a Cartesian coordinate system in order to enable subsequent analysis. Ground clutter is the pattern of radar echoes from fixed ground targets (Rinehart 2010, p. 425). Ground clutter present in the radar images produces anomalously large reflectivity values and near-zero velocity measurements beyond what actually occurred in the snowband. Before the ground clutter could be removed, certain radar data has to be converted from the native format to one that the radar editing program could read. RADX (Dixon 2010) and Radar Software Library (RSL) (Merrit and Wolff 2015) are used to convert raw DOW and UND data to swp format, which is the format required for the radar data editing program SOLO II (NCAR/ATD 2009). DOW data are already in swp format by default. The radar images are examined manually to ensure that the ground clutter present was removed. The criteria for detecting and removing ground clutter for both radars is: any reflectivity radar gate greater than or equal to 15.9 dB combined with any velocity gate that is between -0.5 and 0.5 m s^{-1} and not within the zero isodop. Removing ground clutter is critical because otherwise the associated near-zero velocities

would cause anomalous divergence/convergence signatures that would corrupt multi-Doppler retrievals.

The DOW data also requires three additional steps. The first step is rotating the azimuth angles of the data to properly align such that 0° azimuth points northward. The second additional step is multiplying the DOW radar velocity data by -1. The DOW raw wind data has the opposite sign convention (relative to what is typically used) for radial velocity and multiplying all velocity values by -1 ensures that the data, and thus the wind direction, is accurate. The radial velocity data from other radar sites, as well as atmospheric soundings, are used to verify the correct wind directions and speeds. For the third additional step, noisy radial velocity values are removed using normalized coherent power (NCP). NCP indicates the coherency of received signal phases, and is useful in determining noise in radar data (Satoh and Wurman 2003). NCP ranges from 0-1 (unitless) and high NCP values indicate valid signal and low values indicate noise or atmospheric turbulence (Dixon and Hubbert 2012). For DOW velocity data, any areas with NCP values below 0.2 are removed. Isolated noisy gates outside the main area in the form of ‘speckles’ are removed using a despeckle command in SOLO II software (NCAR/ATD 2009).

Aliased radial velocity is present in both the DOW and UND velocity data. Velocity aliasing occurs when the detected scatterers are moving faster than the maximum unambiguous velocity. The maximum unambiguous velocity (Nyquist velocity) is given by

$$V_{max} = \frac{\pm PRF\lambda}{4}, \quad (6)$$

where PRF is the radar pulse repetition frequency (Rinehart 2010, p. 117-120). On a radar PPI image, radial velocity aliasing is evident where the radial velocity value abruptly switches sign without passing through 0 m s⁻¹.

Velocity data are dealiased using SOLO by first identifying the true 0 m s^{-1} radial velocity contour, which passes through the radar origin. Then, the radar Nyquist velocity (Table 6) is used in a SOLO editing command to dealias the data. Since the environmental wind velocities during this study were much greater than the Nyquist velocity for both radars, there are certain areas of data that are aliased two to four times.

For certain DOW radar elevations, the 0 m s^{-1} contour cannot be followed beyond a certain range. In instances where the contour cannot be followed, radar-to-radar intercomparisons aided in determining the approximate location and shape of the 0 m s^{-1} contour (Fig. 2). For example, dealiased UND radial velocities are used to help determine the location and shape of the 0 m s^{-1} contour in certain DOW velocity plots. DOW velocity plots can then be dealiased with greater accuracy.

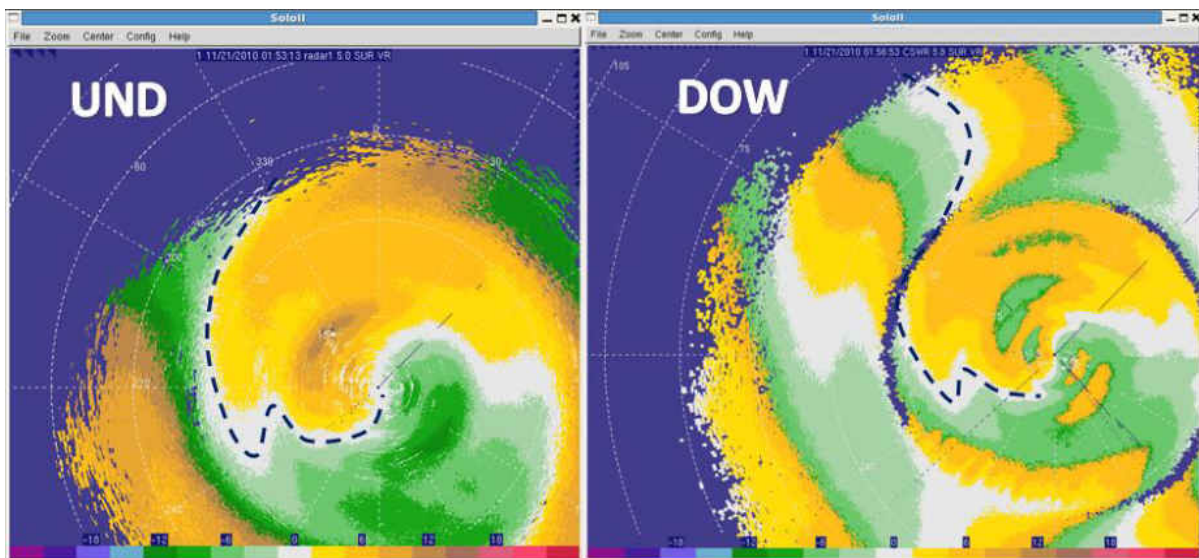


Fig. 2. Example of UND and DOW radial velocity plot before dealiasing in SOLO. The black dashed line indicates the location of the 0 m s^{-1} contour to the left of the individual radar location.

Data in areas where the 0 m s^{-1} contour still cannot be accurately determined even with the help of other radars are removed so that they would not contaminate multi-Doppler

velocity fields. For the DOW, velocity data are removed for ranges exceeding 90 km, 75, 60, 50, and 40 km for the 2.3°, 2.8°, 3.3°, 3.8°, and 4.8° PPI elevation angles, respectively (Fig. 3).

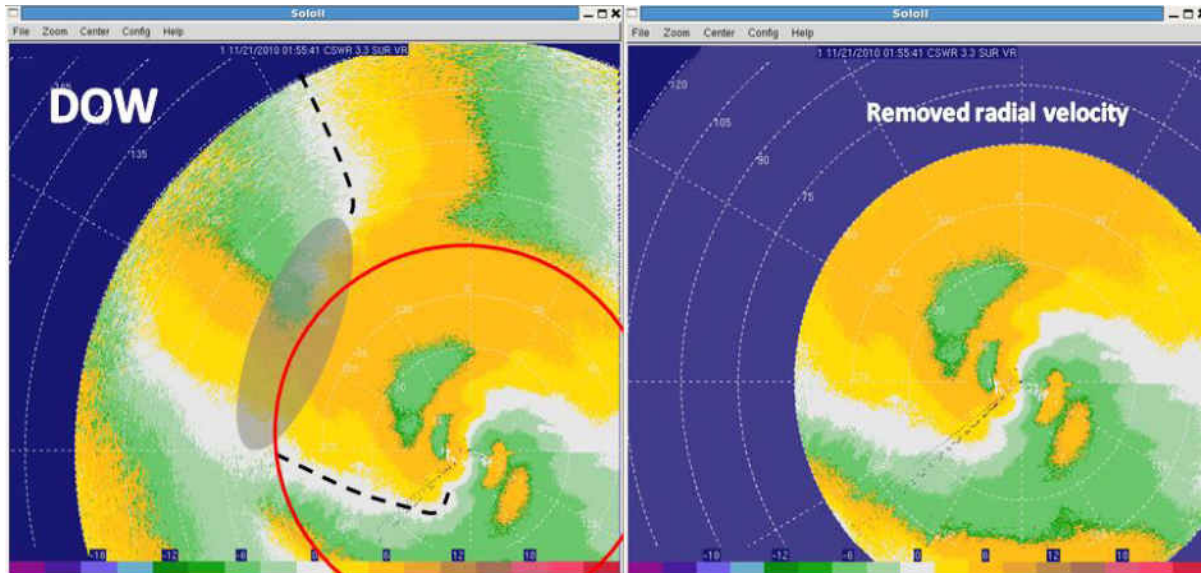


Fig. 3. Radial velocity plots before dealiasing from DOW radar. In the left figure the dashed line indicates the known 0 m s^{-1} isodop while the grey oval indicates the area where the exact location of the 0 m s^{-1} isodop is not known. The red circle encompasses the velocity data that were retained. The right figure shows the same velocity plot with all velocity data beyond 60 km removed.

Radar Format Conversion and Objective Analysis

All of the swp files for both radars are converted to Universal Format (uf) using SOLO software for use in the NCAR program Reorder (Oye and Case 1995). However, there are issues in this process in that the uf volume scan number changes with elevation and the sweep mode number is incorrect. Additional scripts are used to correct these problems.

Reorder is then used to produce estimates at Cartesian coordinates and, thus, to create constant altitude plan position indicator (CAPPI) images. The coordinate system directions used are X (eastward direction), Y (northward direction), and Z (upward height). In Reorder the user sets three parameters called Glongitude, Glatitude, and Galtitude. For this study the Glongitude, Glatitude, and Galtitude are set to a center location corresponding to a central

location between the UND, DOW, and local NEXRAD radar station. The location and altitude used for these three parameters are 47.68814°, -97.03974°, and 0.287 m to set the grid origin coordinates. Three other variables called Rlongitude, Rlatitude, and Raltitude are changed depending upon each radar's longitude, latitude, and altitude.

The radius of influence (RoI) used for this project increases as a function of range. Increasing the RoI with increasing distance is designed to account for the spread of the data at larger ranges (Askelson et al. 2000, Shapiro et al. 2010). The three RoI variables used are $\delta\theta$ (degrees), which specifies the delta-azimuth component of the RoI calculation, $\delta\phi$ (degrees), which specifies the delta-elevation component of the RoI, and the δr (km), which specifies the delta-range component of the RoI. The equation to calculate the arc length distance as a function of range is

$$dX, dY = r(\delta\theta, \delta\phi) * \frac{\pi}{180^\circ}, \quad (7)$$

where r (km) is a function of range. The RoI used is

$$R^2 = dX^2 + dY^2 + dZ^2, \quad (8)$$

with the Cressman weight function (Cressman 1959) used as the weighing function for this study. When using the Cressman weight function, the weight for a certain radar gate value (W) is calculated using

$$W = \frac{R^2 - r^2}{R^2 + r^2}, \quad (9)$$

and r^2 is the square of the distance between the gate and the grid point (Oye and Case 1995).

Artifacts Arising from Multi-Doppler Objective Analysis Process

Early attempts at processing the data produced concentric rings around each radar location in the dual Doppler velocity images (Fig. 4). The rings are an artifact from the objective analysis process where the different radar elevation angles intersected the ROI sphere when using the Cressman weight function. A limited number of elevation angles and vertical wind shear in the atmosphere also contribute to this artifact. A small ROI intersects data from higher and lower elevations in an oscillating fashion. The values at these intersections are then estimated on CAPPIs, creating rings of larger and then smaller velocity values around each radar location. The default $\delta\theta$, $\delta\phi$, and δr values in Reorder used early on did not amount to enough smoothing, thus the rings were present. Larger values were tested for $\delta\theta$, $\delta\phi$, δr , and through experimentation values that smoothed out the rings were selected. The rings are smoothed out because they create the illusion of waves in the atmosphere and cause incorrect wind vectors. The smoothing also slightly affects the reflectivity parameter as well. Such rings have also been observed by Nissen et al. (2001) while retrieving the three-dimensional wind field for stratiform snow events.

Reorder values of 5.5 km for dX, dY, and dZ have been found to smooth out the rings in the data (Table 7). It is possible that the amount of smoothing needed to eliminate the rings also eliminates smaller scale features. This issue may be more common than reported, as stronger velocities from convective storms could overpower the rings making them unseen.

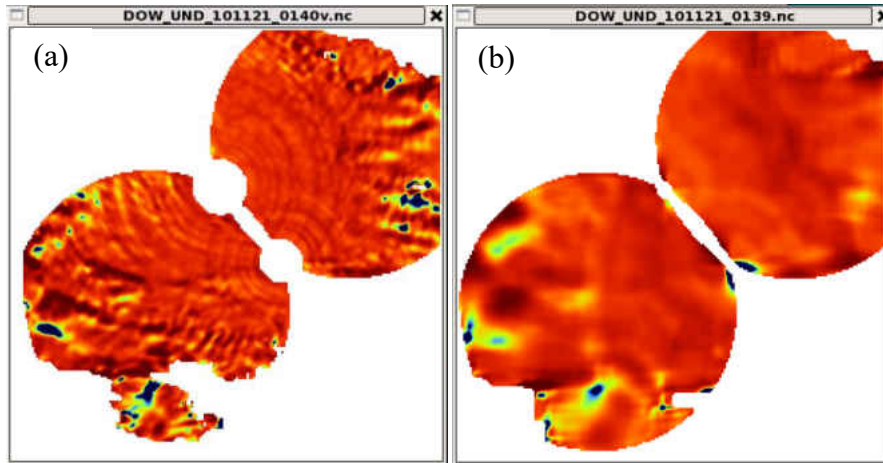


Fig. 4. CAPPI images of w at 3.0 km from dual-Doppler analysis showing (a) anomalous circles and (b) w after additional smoothing was applied to remove these circles. Values range from -4 to 4 m s^{-1} . Images created with Ncview (Pierce 2003).

Table 7. Default and chosen radius of influence values used in Reorder (degrees for $\delta\theta$ and $\delta\phi$, km for δr).

	Radius of Influence Values		
	δr	$\delta\phi$	$\delta\theta$
Default	1	1.8	1.8
Used	5.5	5.5	5.5

Multi-Doppler Wind Retrieval

Multi-Doppler processing uses multiple Doppler radars to retrieve the three-dimensional wind field from radial velocity data. In so doing, the wind flow field, and in particular the updrafts and downdrafts, may be analyzed in relation to the snowbands. There are four unknowns that must be solved for to use in four equations to determine the wind field: u , v , w , w_t . The unknowns u , v , w , are the components of velocity in x , y , and z directions, and w_t is the precipitation terminal velocity (Rinehart 2010, p. 223-224).

Using two Doppler radars with the flat Earth assumption, the horizontal and vertical wind components at every point within the dual-Doppler lobes can be derived using a combination of Doppler velocity value observations from the two radars in addition to a

reflectivity-terminal velocity relationship and the anelastic mass continuity equation. The anelastic mass continuity equation is

$$\frac{\partial u}{\partial x} + \frac{\partial v}{\partial y} + \frac{\partial w}{\partial z} - \kappa w = 0, \quad (10)$$

where κ is the logarithmic spatial rate of change of density with height. The anelastic mass continuity equation is used to estimate a value for w . The equations for u and v are

$$u = \frac{R_1 V_1 (y - y_2) - R_2 V_2 (y - y_1) - w_t [(z - z_1)(y - y_2) - (z - z_2)(y - y_1)]}{(x - x_1)(y - y_2) - (x - x_2)(y - y_1)}$$

$$- w \frac{[(z - z_1)(y - y_2) - (z - z_2)(y - y_1)]}{(x - x_1)(y - y_2) - (x - x_2)(y - y_1)} = C_1 - w C_2, \quad (11a)$$

and

$$v = \frac{R_2 V_2 (x - x_1) - R_1 V_1 (x - x_2) - w_t [(z - z_2)(x - x_1) - (z - z_1)(x - x_2)]}{(x - x_2)(y - y_1) - (x - x_1)(y - y_2)}$$

$$- w \frac{[(z - z_2)(x - x_1) - (z - z_1)(x - x_2)]}{(x - x_2)(y - y_1) - (x - x_1)(y - y_2)} = C_3 - w C_4, \quad (11b)$$

where

$$R_i = [(x - x_i)^2 + (y - y_i)^2 + (z - z_i)^2]^{0.5}, \quad (12)$$

and

$$V_i = \frac{u(x - x_i)}{R_i} + \frac{v(y - y_i)}{R_i} + \frac{(w + w_t)(z - z_i)}{R_i}, \quad (13)$$

where V_i is the measured radial velocity related to the Cartesian wind components. To find just the value of w the particle terminal velocity is removed. Using a linear, inhomogeneous, hyperbolic partial differential equation, the vertical air motion w can be obtained (following, e.g., Armijo 1969):

$$-C_2 \frac{\partial w}{\partial x} - C_4 \frac{\partial w}{\partial y} + \frac{\partial w}{\partial z} = w \left(\frac{\partial C_2}{\partial x} + \frac{\partial C_4}{\partial y} + \kappa \right) - \left(\frac{\partial C_1}{\partial x} + \frac{\partial C_3}{\partial y} \right). \quad (14)$$

Setting the boundary condition $w = 0 \text{ m s}^{-1}$ with (14) at $z = 0$ would involve upward integration while setting $w = 0 \text{ m s}^{-1}$ at the analysis domain top (at or above feature echo top) would involve downward integration. Using (14) solutions result in an anelastic wind field synthesis in Cartesian coordinates where the horizontal wind components are used to compute the vertical wind components. Errors in the horizontal wind components accumulate during integration causing more error at the top (bottom) of the boundary condition when using upward (downward) integration. Other errors that affect the vertical wind components include incorrect storm motion estimates and finite data collection time which result from combining inappropriate divergence values. To represent realistic values of w , two boundary conditions are implemented, one at the bottom of the domain and at the storm top (where “storm” refers to any weather feature observed by the radar). At these boundary conditions $w = 0 \text{ m s}^{-1}$ and then a Boussinesq approximation is applied to the vertically integrated horizontal divergence as an integral constraint:

$$C = \int_0^{z_T} \left(\frac{\partial u}{\partial x} + \frac{\partial v}{\partial y} \right) dz = - \int_0^{z_T} \frac{\partial w}{\partial z} dz, \quad (15)$$

where z_T is the storm top and C is a constant. This necessitates the integrated horizontal divergence be equal to the constant and w above the storm to go to 0 m s^{-1} . This can be called the variational integral constraint (Ray et al. 1980).

Multi-Doppler Velocity Retrievals

The NCAR Custom Editing and Display of Reduced Information in Cartesian space (CEDRIC) (Miller and Fredrick 2009) program is used to estimate the three dimensional wind field using equations and techniques described in **Multi-Doppler Wind Retrieval**.

The CEDRIC program requires the storm advection speed and direction along with a reference time. These three variables are specified by the user and the advection speed and direction are used to accurately translate radar data to the positions this data would have at the reference time. Upward integration with variational integral constrain are used, the details of which are also described in **Multi-Doppler Wind Retrieval**. For this study, since the snowbands did not have cloud tops higher than about 10 km, and the aircraft did not fly higher than 4.5 km, upward integration was used with variational adjustment on w . Finally a script was used to convert the output ced-format files to NetCDF, so these NetCDF files can be used with a radar display program.

The terminal velocity estimate used in CEDRIC (vt) is calculated using

$$vt = -A * 10.0^{0.1*Z*B} * \left(\frac{RHO(0)}{RHO(Ht)} \right)^C$$

$$A = 1.5 \tag{16}$$

$$B = 0.105$$

$$C = 0.4$$

and

$$RHO = EXP(-Ht * 0.1), \tag{17}$$

where Z is radar reflectivity (dBZ), RHO is air density, and Ht is height (km). Rain and ice have different constant values from Joss and Waldvogel (1970) and Atlas et al. (1973).

Aircraft Data Analysis

Data from the UND Citation Research Aircraft are displayed using the program Cplot2 (Delene et al. 2015). Cplot2 allows aircraft data to be displayed on plots with customizable x and y variables. Cplot2 is used to display size distributions of hydrometeors inside versus outside a snowband, in addition to environmental temperature, wind velocity,

and aircraft altitude. Size distribution plots are used to visualize all of the channels from the 2DC probe and to evaluate how hydrometeor number concentration is related to hydrometeor size. Concentration measurements are normalized over the size interval of the instrument channel to take into account different hydrometeor size intervals. Normalizing over the size interval also allows comparison between different bins from different instruments.

Finally aircraft flight transects in longitude and latitude (decimal degrees) were converted to Cartesian coordinates (kilometers) using Python with the Basemap module. Hydrometeor images from the 2DC were selected by images that corresponded with the average time of the particular aircraft transect.

Radar Imaging Software

Radar image data are displayed using Cutsome, an IDL-based GUI software program written by Jean-Pierre Aubagnac, Brent Gordon, Mark Askelson, and Adam Theisen. With Cutsome, one can read in NetCDF files, plot multiple parameters on a single image, generate radar cross sections images, overlay aircraft flight transects, and generate images to postscript files.

In Cutsome, storm relative correction is applied to the aircraft flight transect so that the aircraft transect is relative to the radar data at a reference time. The storm speed, direction, and the reference time used in the CEDRIC program were used for storm-relative correction in Cutsome. Aircraft transects were then overlaid on Cutsome plots.

Radar-Aircraft Transect Analysis

Dual polarization radar analyses along the aircraft transect are conducted with the DOW and UND radar data. To determine the radar parameter values associated with the particular aircraft location, the aircraft transect locations are advected relative to the radar

using storm-relative correction. This step requires the storm propagation direction, speed, the average of the aircraft flight transect start and end times, and a radar reference time. The radar reference time is the average time of each particular aircraft flight transect, using the transect start and end times. The positions along the aircraft transect are then moved relative to the radar reference time. The amount a position along the aircraft transect moves is calculated based on the difference between the aircraft time and the radar reference time. In the Reorder software, the user has the option to set the output altitude interval(s). For the radar-aircraft transect analysis, the aircraft altitude is used as the Reorder program output altitude. Trilinear interpolation is used to estimate values along the aircraft transect. Finally the average radar parameter value for each particular transect is computed.

CHAPTER III

RESULTS

Certain time intervals along the entire aircraft flight track are used to compare hydrometeor characteristics inside a snowband with characteristics outside a snowband. These time intervals are selected by identifying intervals during which the aircraft is being flown at a relatively constant altitude and heading. With data being collected by the aircraft along a level flight path, the sampled snowband characteristics are more likely to be constant. For this study, the aircraft was not flown in a way so as to follow the snowband, rather the aircraft was flown over the same general location while the snowband progressed through the region. Because of the slow snowband progression and the limited region in which the aircraft was flown, observations outside of the snowband were collected about one hour after observations were collected inside the snowband. A ‘transect’ refers to one aircraft track from start to end. A ‘transect-pair’ is defined to be two straight transects flown at the same altitude, with one transect occurring inside the snowband and one outside the snowband after the snowband propagated away.

Data for this study were collected on 20-21 November 2010. While this study focuses on the snowband from approximately 1 – 3 UTC 21 November 2010, areas of banded precipitation became visible on radar in central North Dakota as early as 8 UTC 20 November and would persist until nearly 10 UTC 21 November. However only between 1 – 3 UTC 21 November were both the radars and aircraft sampling. For this study, a

snowband is defined as being ellipsoidal in shape, having at least a 2-to-1 horizontal length to width ratio, persist for at least two hours, and containing reflectivities that are at least 3 dB (doubling linear power) greater than surrounding values. The general width of a snowband that meets the criteria above for this time period is 20 – 30 km, which is Meso- γ scale (Thunis and Bornstein 1996). To enable comparison of characteristics inside and outside of a snowband, certain reflectivity thresholds are used to adjust the aircraft transects to delineate snowband boundaries (Table 8). These thresholds are used to determine whether the aircraft transect is inside a snowband core, outside the snowband, or along the edge of a snowband. Unless otherwise specified, when an aircraft transects the snowband, “inside” means within the snowband core.

Table 8. Reflectivity values used to distinguish if the aircraft was in the snowband core, along the snowband edge, or outside the snowband.

Radar	Outside	Edge	Core
DOW	Less than 10 dBZ	10 – 12.49 dBZ	Greater than 12.49 dBZ
UND	Less than 7 dBZ	7 – 9.9 dBZ	Greater than 9.9 dBZ

During the aircraft sampling period, the main snowband was oriented roughly W – E and propagating towards the northeast. None of the analyzed transect-pairs are associated with rain-detection from surface weather stations and the closest sounding from Bismarck, ND showed the temperature readings at all levels were below 0°C. Because rain was not detected and a sounding showed freezing temperatures at all levels, melting snow was not prevalent. Radar and microphysical characteristics associated with melting snow will not be considered in this study.

Aircraft Results

The transect-pair for the first set of aircraft results (Fig. 5) occurs at 2.71 km AGL. Again the hydrometeor size (herein called diameter) is determined from a particle

reconstruction method described in Appendix A. From the starting measurement capability of the 2DC probe to roughly 300 μm diameter, the cloud particle concentrations inside and outside the snowband are very similar. Between 300 μm to 900 μm the concentration outside the snowband is greater than inside the snowband. From 900 μm to roughly 2800 μm the concentration is higher inside the band. For concentration measurements both inside and outside the snowband, a concentration increase occurs after the initial decrease which forms a peak. The peak in cloud concentration outside the snowband of $1.9 * 10^{-5} \# \text{cm}^{-3} \mu\text{m}^{-1}$ is at roughly 400 μm , while the peak inside the snowband occurs at $0.5 * 10^{-6} \# \text{cm}^{-3} \mu\text{m}^{-1}$ between 1000 and 1400 μm . The hydrometeor images from the 2DC instrument show larger, more aggregated hydrometeors inside the snowband (Fig. 5b), and smaller, rounder hydrometeors outside the snowband (Fig. 5c).

For the second set of aircraft results, the transect-pair occurs at 2.41 km AGL (Fig. 6). Again, from the starting measurement capability of the 2DC to 300 μm diameter, the cloud particle concentrations inside and outside the snowband are very similar. Between 300 μm to roughly 1100 μm the concentration outside the snowband is greater than inside the snowband. From roughly 1100 μm to 2800 μm the concentration is higher inside the band. The peak in cloud concentration outside the snowband is $1 * 10^{-5} \# \text{cm}^{-3} \mu\text{m}^{-1}$ at 400 μm , while there were two peaks inside the snowband with values of roughly $0.8 * 10^{-6} \# \text{cm}^{-3} \mu\text{m}^{-1}$ at 900 μm and at 1200 μm . Again, 2DC images show larger, more aggregated hydrometeors inside the snowband (Fig. 6b), and with smaller hydrometeors outside the snowband (Fig. 6c).

The third transect-pair (Fig. 7) at 1.80 km AGL is very similar to the first transect. The cloud particle concentrations inside and outside the snowband are very similar from the

starting measurement capability of the 2DC to 300 μm diameter. Between 300 μm to roughly 900 μm the concentration outside the snowband is greater than inside the snowband. From roughly 900 μm to 2800 μm the concentration is higher inside the band. The peak in cloud concentration outside the snowband is $2.5 * 10^{-5} \# \text{cm}^{-3} \mu\text{m}^{-1}$ at 425 μm , while the peak inside the snowband occurs at $2 * 10^{-6} \# \text{cm}^{-3} \mu\text{m}^{-1}$ at roughly 1000 μm . Larger, aggregated hydrometeors are shown inside the snowband (Fig. 7b), and smaller, round hydrometeors outside the snowband (Fig. 7c).

The fourth transect-pair occurs (Fig. 8) at 1.19 km, and is where the results start to change. From the starting measurement capability of the 2DC to 400 μm diameter, the cloud particle concentrations inside the snowband are slightly larger than outside the band, with a small peak at $6 * 10^{-5} \# \text{cm}^{-3} \mu\text{m}^{-1}$ around 150 μm . Between 400 μm to 700 μm the concentration outside the snowband is slightly greater than inside the snowband. From roughly 700 μm to 2800 μm the concentration is higher inside the band. Measurements outside the snowband do not have a definite peak. The second peak inside the snowband occurs at $2.5 * 10^{-6} \# \text{cm}^{-3} \mu\text{m}^{-1}$ at a diameter slightly greater than 1000 μm . Larger, aggregated hydrometeors are shown inside the snowband (Fig. 8b), and hydrometeors that are generally smaller and rounder and shown outside the snowband (Fig. 8c).

For the fifth and final transect-pair (Fig. 9) at 0.89 km, for sizes ranging from the starting measurement capability of the 2DC to slightly less than 300 μm diameter, the cloud particle concentrations inside and outside the snowband are very similar. Between roughly 300 μm to 900 μm the concentration outside the snowband is greater than inside the snowband. From roughly 900 μm to 2800 μm the concentration is higher inside the snowband, however the concentration difference between inside/outside for this transect-pair

is not as great as the difference in previous plots. Again measurements outside the snowband do not have a definite peak, while inside the snowband a small peak occurs at roughly 900 μm with a peak value of $0.5 * 10^{-6} \# \text{cm}^{-3} \mu\text{m}^{-1}$. Larger, aggregated hydrometeors are shown inside the snowband (Fig. 9b), and smaller, round hydrometeors outside the snowband (Fig. 9c).

Hydrometeor size and concentration distributions change depending on altitude. Inside the snowband, the maximum hydrometeor size is roughly the same for all five sampled altitudes; however the concentration of hydrometeors above 1000 μm decreases with decreasing altitude. For hydrometeors outside the snowband, the maximum size at the highest sampled altitude (2.71 km AGL) is $\sim 1600 \mu\text{m}$, while the maximum size at the lowest altitude (0.89 km AGL) is $\sim 2800 \mu\text{m}$. Concentrations of larger hydrometeors inside the snowband decrease as altitude decreases, while concentrations of larger hydrometeors outside the snowband increase as altitude decreases. At the lowest sampled altitude, the size and concentration distributions inside and outside the snowband are more similar than the distributions at higher altitudes.

Temperatures and vertical velocities measured with the aircraft inside and outside the snowband are quite similar (Table 9). The largest temperature difference between inside and outside the snowband measurements collected at the same height is only 1°C , occurring at 2.71 km. Vertical velocity measurements do not vary by more than 0.2 m s^{-1} inside versus outside the band at all five altitudes. The average vertical velocity across all five altitudes for both inside and outside the snowband is 1.6 m s^{-1} . The average temperature inside the snowband is -10.5°C and the average outside is -10.7°C .

Table 9. Measurements from various transects completed using the Citation Research Aircraft. Time is measured in seconds from midnight (SFM). Altitude (AGL), temperature, and vertical velocity, including standard deviation, are provided. “In” and “Out” indicate within and outside the snowband, respectively.

Aircraft Transect (SFM)		Altitude (m)		Temperature (°C)		Vertical Velocity (m s ⁻¹)	
In	Out	In	Out	In	Out	In	Out
5990.0 - 6181.0	9820.0 - 9988.0	2718.5 ± 2.7	2711.0 ± 4.3	-13.9 ± 0.3	-14.9 ± 0.1	1.7 ± 0.2	1.6 ± 0.2
6252.0 - 6416.0	9609.0 - 9749.0	2417.3 ± 2.1	2407.9 ± 2.2	-12.8 ± 0.1	-12.6 ± 0.1	1.5 ± 0.2	1.5 ± 0.2
6789.0 - 6922.0	9008.0 - 9216.0	1806.3 ± 2.3	1796.4 ± 2.5	-9.0 ± 0.1	-8.8 ± 0.1	1.6 ± 0.2	1.4 ± 0.2
7284.0 - 7399.0	8529.0 - 8678.0	1194.7 ± 2.7	1189.9 ± 1.9	-8.6 ± 0.1	-8.9 ± 0.1	1.6 ± 0.1	1.7 ± 0.2
7531.0 - 7661.0	8255.0 - 8385.0	893.0 ± 3.3	884.0 ± 1.9	-8.1 ± 0.1	-8.3 ± 0.1	1.7 ± 0.3	1.6 ± 0.3

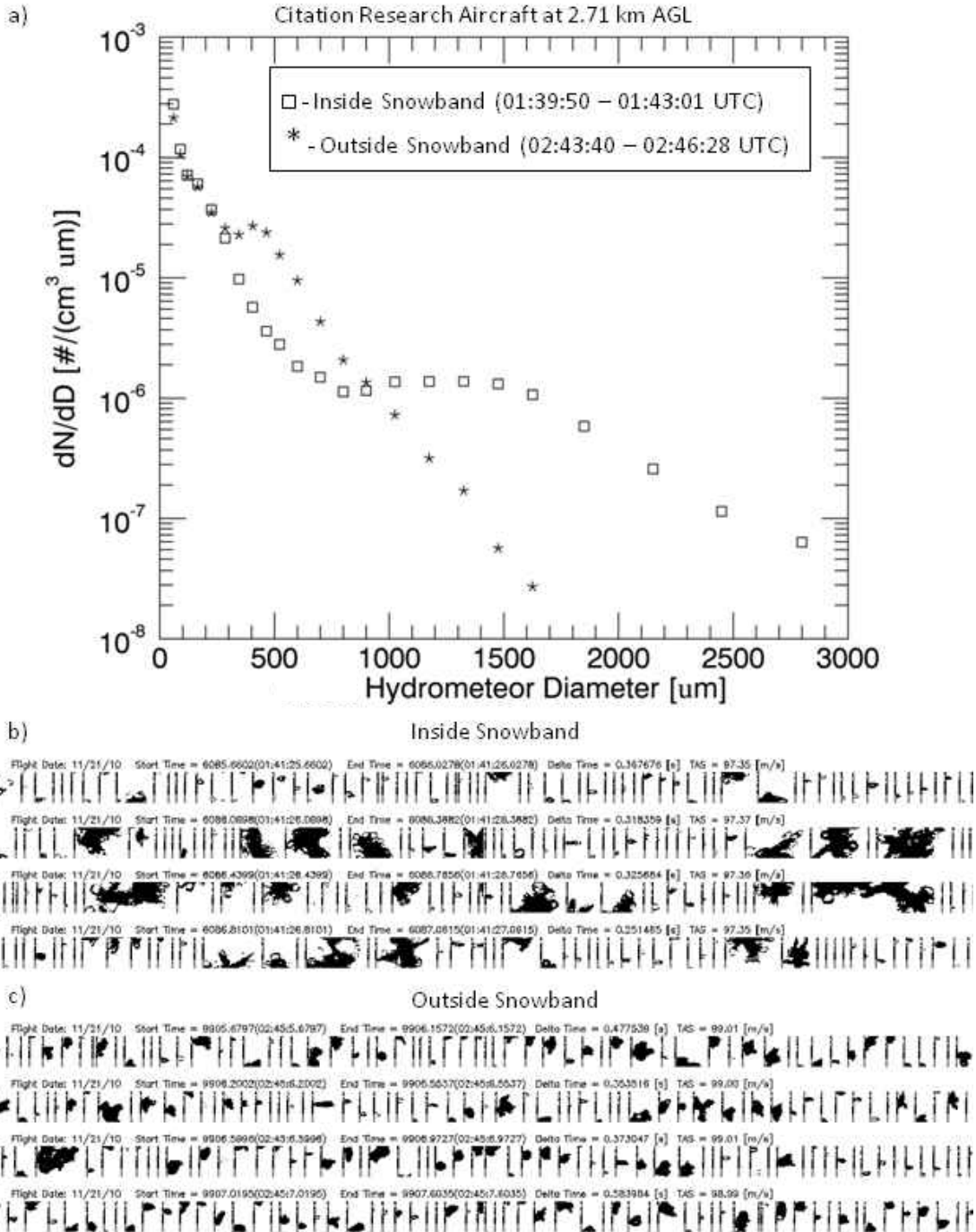


Fig. 5. Aircraft observations from a 2DC probe (a) of cloud particle concentration versus diameter on 21 Nov. 2010 at 2.71 km AGL. The x-axis is the cloud hydrometeor diameter (μm) and the y-axis is the concentration ($\# \text{cm}^{-3} \mu\text{m}^{-1}$) normalized with respect to the bin size interval. Individual bin averages are shown as squares inside the snowband (01:39:50 – 01:43:01 UTC) and stars outside the snowband (02:43:40 – 02:46:28 UTC). Each symbol represents the average of one channel over the time interval. Two-dimensional cloud particle images taken inside (b) the snowband between 01:41:26 – 01:41:27 UTC, and images taken outside (c) the snowband between 02:45:06 – 02:45:07 UTC.

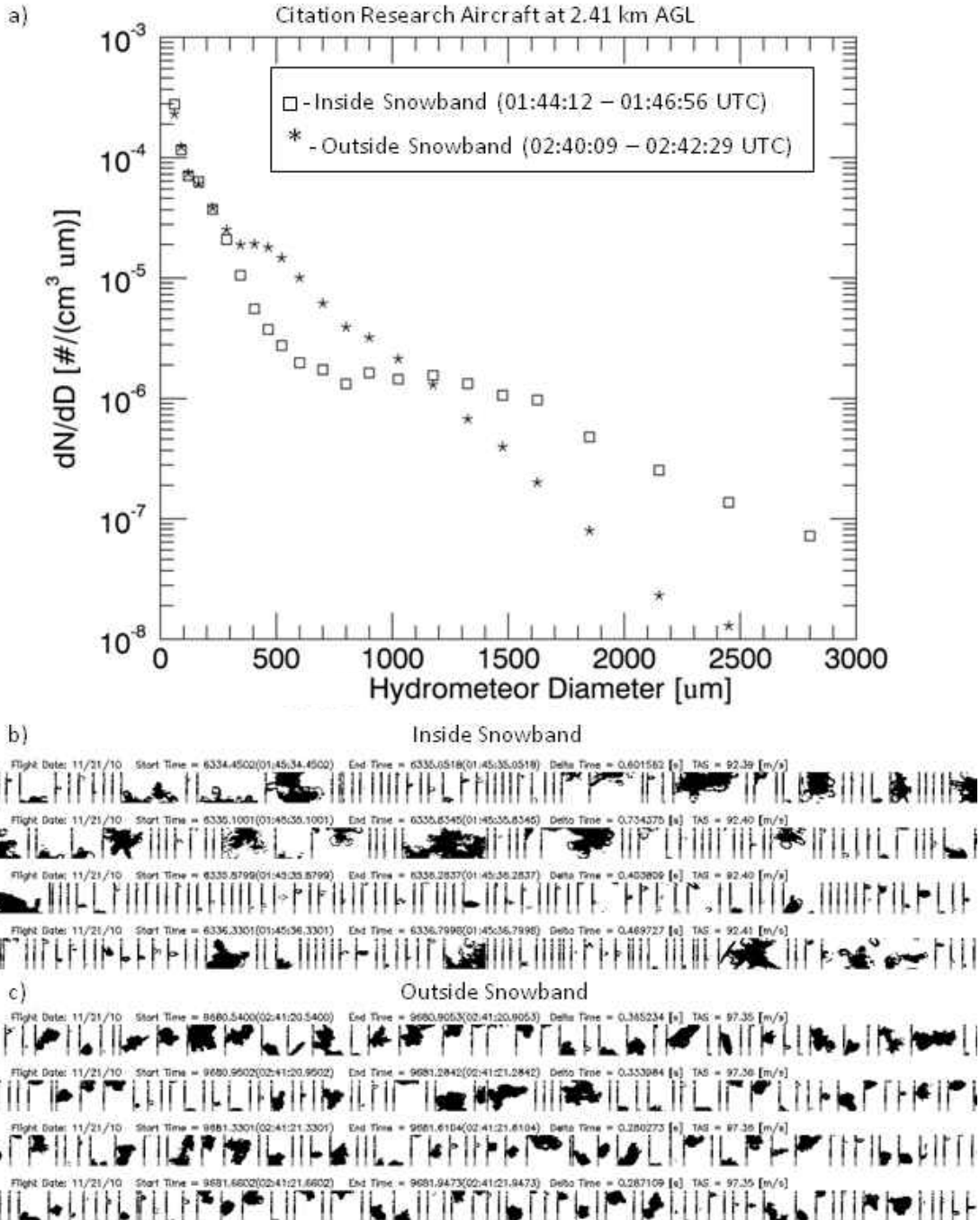


Fig. 6. Aircraft observations from a 2DC probe (a) of cloud particle concentration versus diameter on 21 Nov. 2010 at 2.41 km. The x-axis is the cloud hydrometeor diameter (μm) and the y-axis is the concentration ($\# \text{ cm}^{-3} \mu\text{m}^{-1}$) normalized with respect to the bin size interval. Individual bin averages are shown as squares inside the snowband (01:44:12 – 01:46:56 UTC) and stars outside the snowband (02:40:09 – 02:42:29 UTC). Two-dimensional cloud particle images taken inside (b) the snowband between 01:54:35 – 01:45:37 UTC, and images taken outside (c) the snowband between 02:41:20 – 02:41:21 UTC.

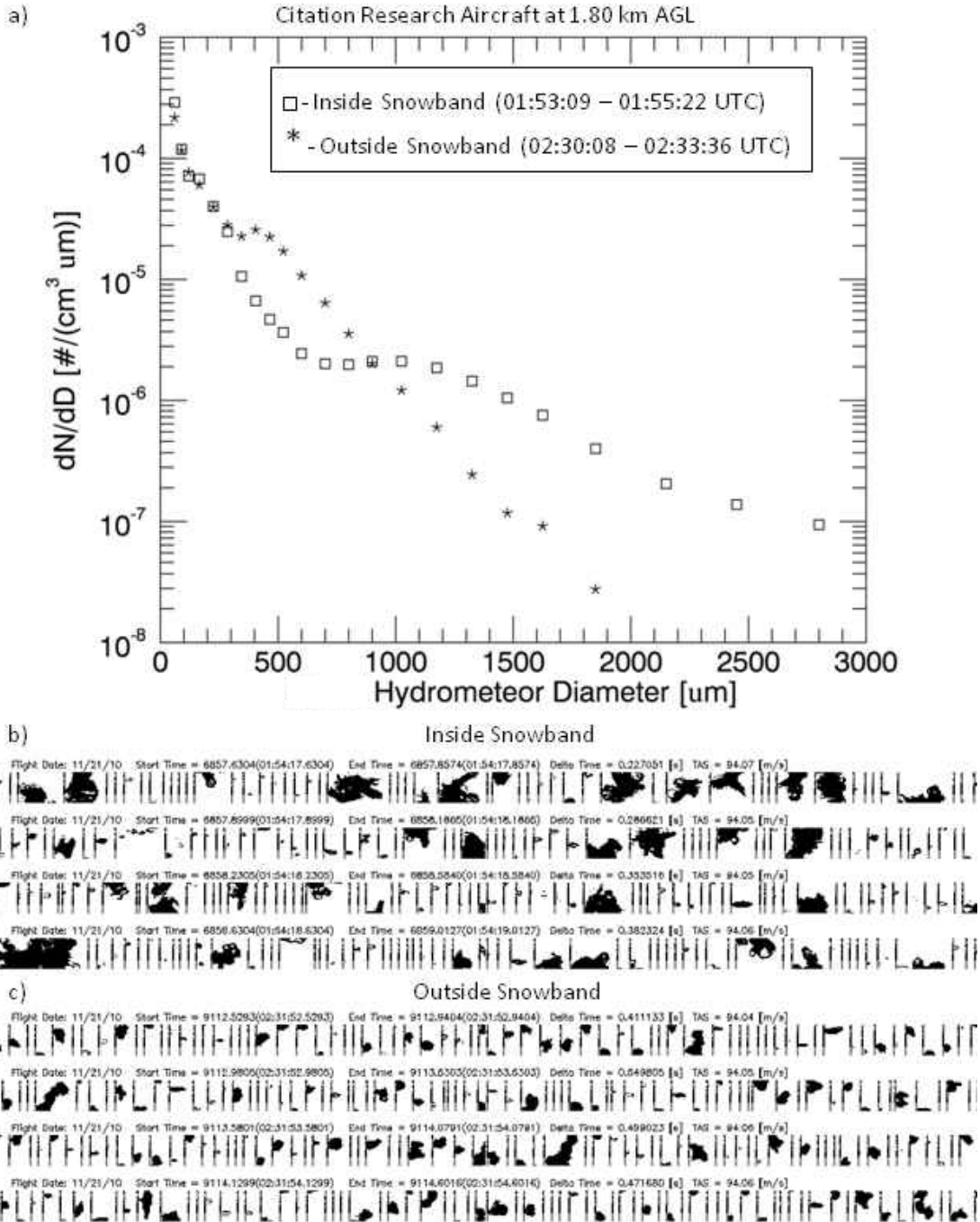


Fig. 7. Aircraft observations from a 2DC probe (a) of cloud particle concentration versus diameter for 21 Nov. 2010 at 1.80 km. The x-axis is the cloud hydrometeor diameter (μm) and the y-axis is the concentration ($\# \text{cm}^{-3} \mu\text{m}^{-1}$) normalized with respect to the bin size interval. Individual bin averages are shown as squares inside the snowband (01:53:09 – 01:55:22 UTC) and stars outside the snowband (02:30:08 – 02:33:36 UTC). Two-dimensional cloud particle images taken inside (b) the snowband between 01:54:17 – 01:54:19 UTC, and images taken outside (c) the snowband between 02:31:52 – 02:31:54 UTC.

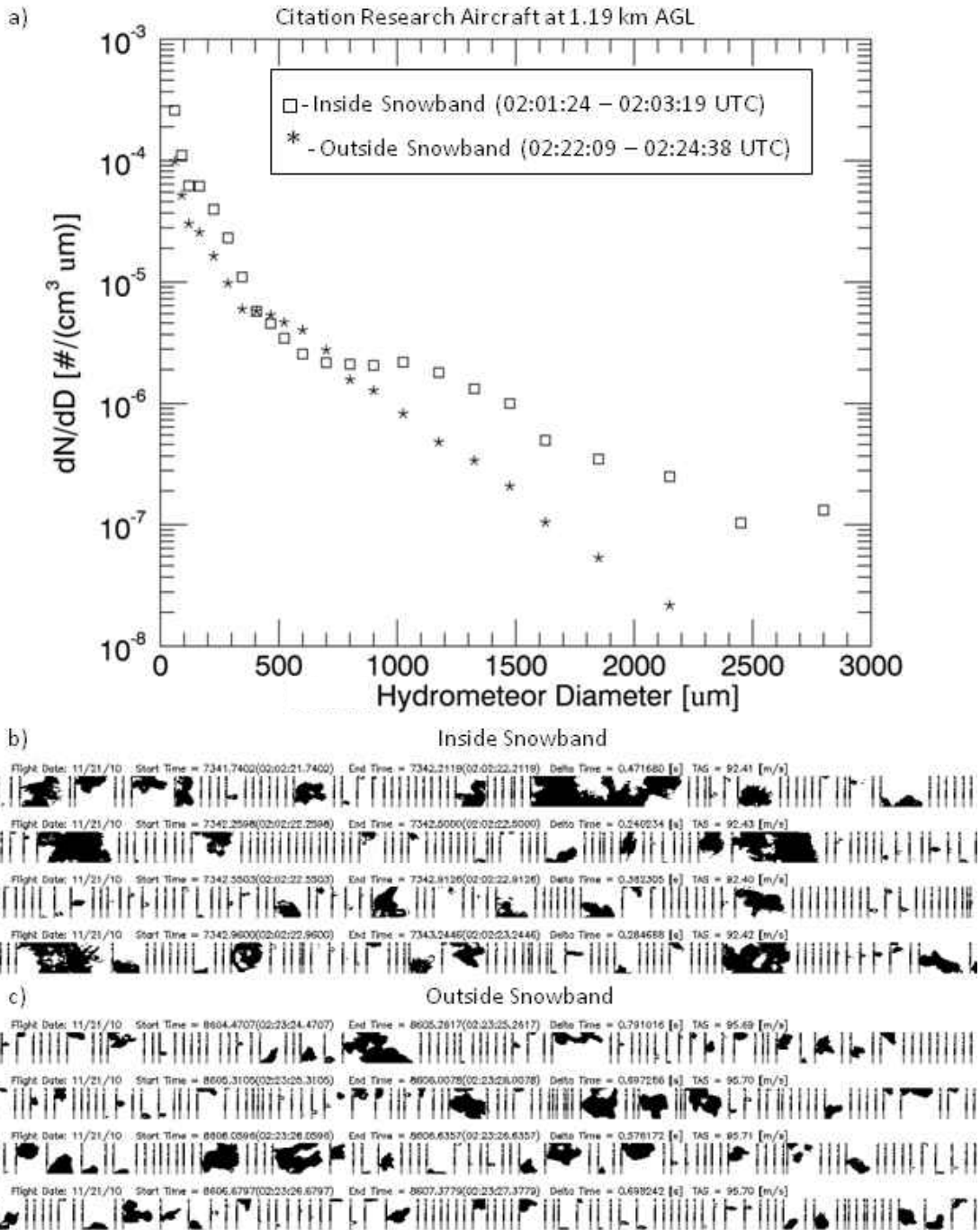


Fig. 8. Aircraft observations from a 2DC probe (a) of cloud particle concentration versus diameter for 21 Nov. 2010 at 1.19 km. The x-axis is the cloud hydrometeor diameter (μm) and the y-axis is the concentration ($\# \text{ cm}^{-3} \mu\text{m}^{-1}$) normalized with respect to the bin size interval. Individual bin averages are shown as squares inside the snowband (02:01:24 – 02:03:19 UTC) and stars outside the snowband (02:22:09 – 02:24:38 UTC). Two-dimensional cloud particle images taken inside (b) the snowband between 02:02:21 – 02:02:23 UTC, and images taken outside (c) the snowband between 02:23:24 – 02:23:27 UTC.

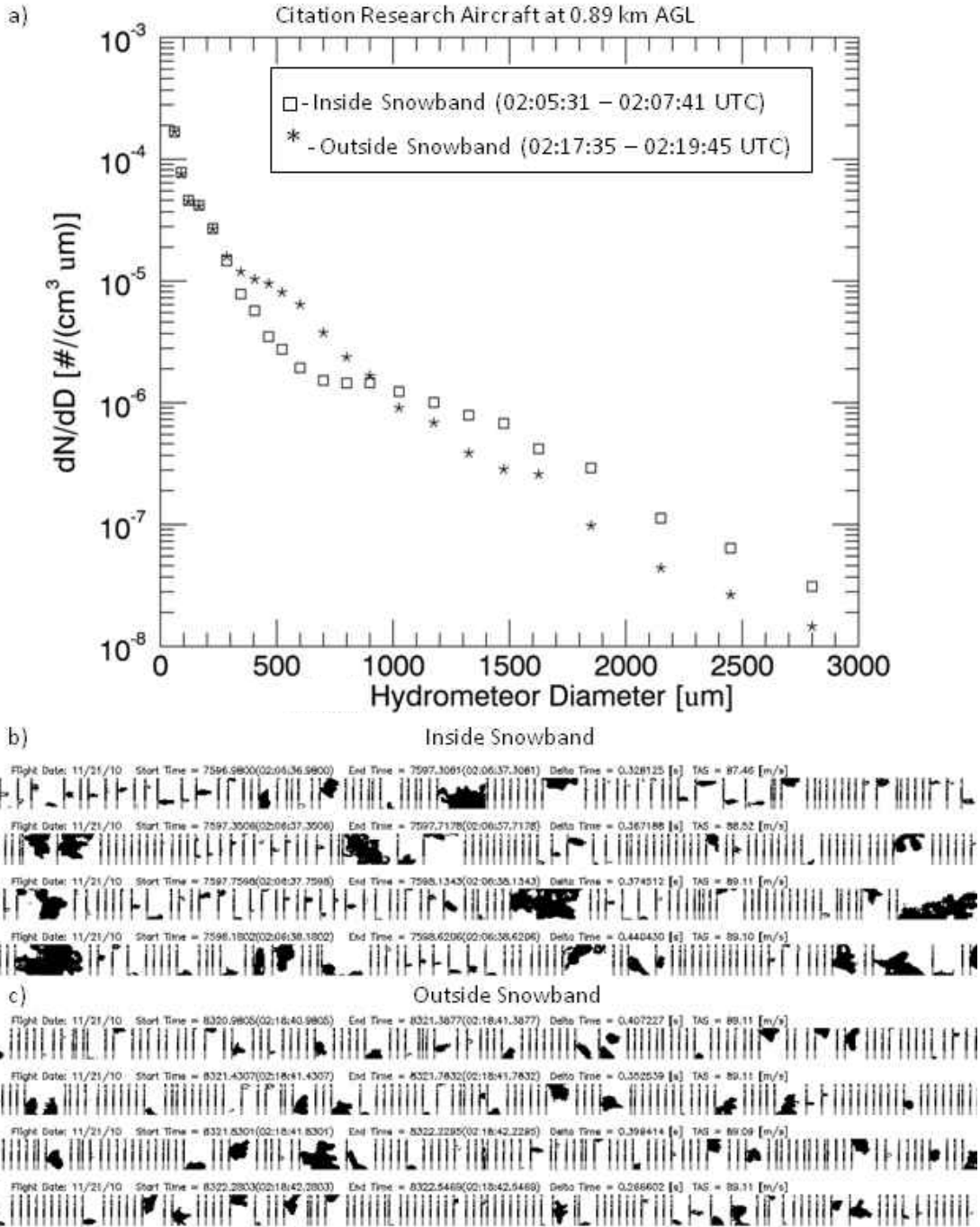


Fig. 9. Aircraft observations from a 2DC probe (a) of cloud particle concentration versus diameter for 21 Nov. 2010 at 0.89 km. The x-axis is the cloud hydrometeor diameter (μm) and the y-axis is the concentration ($\# \text{ cm}^{-3} \mu\text{m}^{-1}$) normalized with respect to the bin size interval. Individual bin averages are shown as squares inside the snowband (02:05:31 – 02:07:41 UTC) and stars outside the snowband (02:17:35 – 02:19:45 UTC). Two-dimensional cloud particle images (b) taken inside the snowband between 02:06:37 – 02:06:39 UTC, and images taken outside (c) the snowband between 02:18:40 – 02:18:42 UTC.

Radar Results

To determine whether the wind direction retrieved with the dual Doppler analyses are correct, dual Doppler data with wind vectors are compared with surface and upper air data. The dual Doppler analysis at 01:42:34 UTC (Fig. 10) shows that the left lobe has wind vectors coming from approximately 90° close to the dual Doppler analysis baseline, and then shifting to approximately 135° further south. This agrees with surface and upper air data as a surface observation at the Grand Forks Airport at 01:53 UTC had wind coming from 80° . Sounding data from Bismarck, ND, at 00 UTC on 21 November 2010 had a wind coming from 90° at 0.5 AGL, with the coming wind shifting direction to the southwest within the first four km above ground (Plymouth State Weather Center). Thus, the dual Doppler retrieved wind analysis is in agreement with measured wind direction values.

As indicated earlier, a transect-pair involves two straight transects at the same altitude, one inside the snowband and one outside the snowband (a ‘transect’ refers to one aircraft track from start to end inside or outside of a snowband). CAPPIs closest to the respective transect heights inside and outside the snowband for each transect-pair are shown in Fig. 11.

Upon close inspection, there exists a bias between the vertical velocity values from the aircraft, and the vertical velocity values retrieved by the dual-Doppler analysis. The aircraft vertical velocity data is always $\sim 1 \text{ m s}^{-1}$ greater than the values from the dual-Doppler analysis. This bias between aircraft and dual-Doppler data was discovered when vertical velocity values along multiple aircraft transects were compared to corresponding values from the dual-Doppler analysis. This bias has *not* been used to adjust any data in this research, however areas where the bias could strongly affect the data are noted.

11/21/10 DOW UND 01:42:34 UTC CAPPI HEIGHT=0.5 km

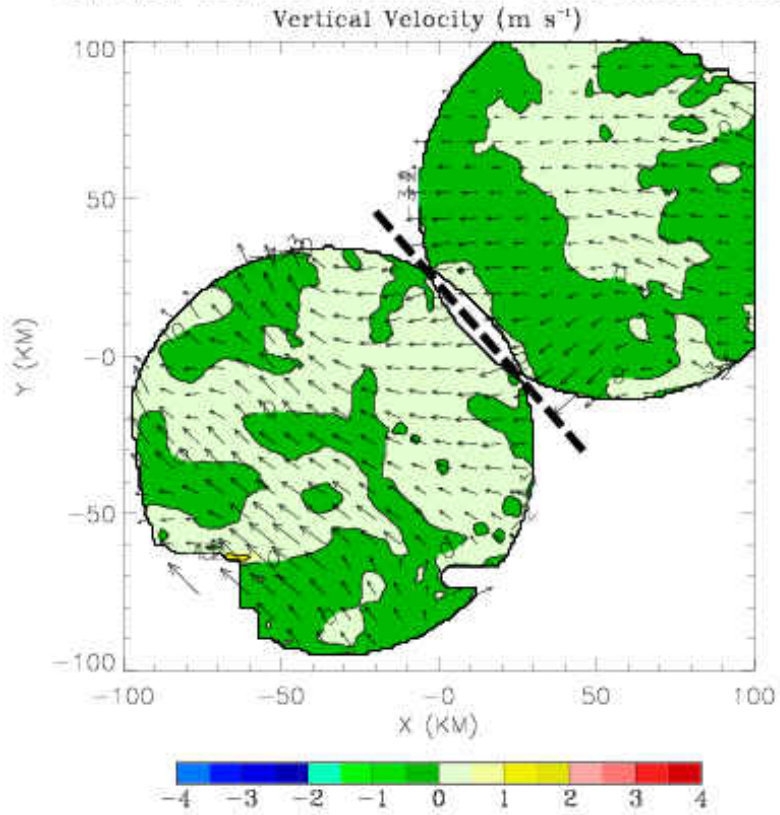


Fig. 10. CAPPI plot of retrieved vertical velocity at 0.5 km with horizontal wind vectors. The dashed line shows the baseline between the two radars.

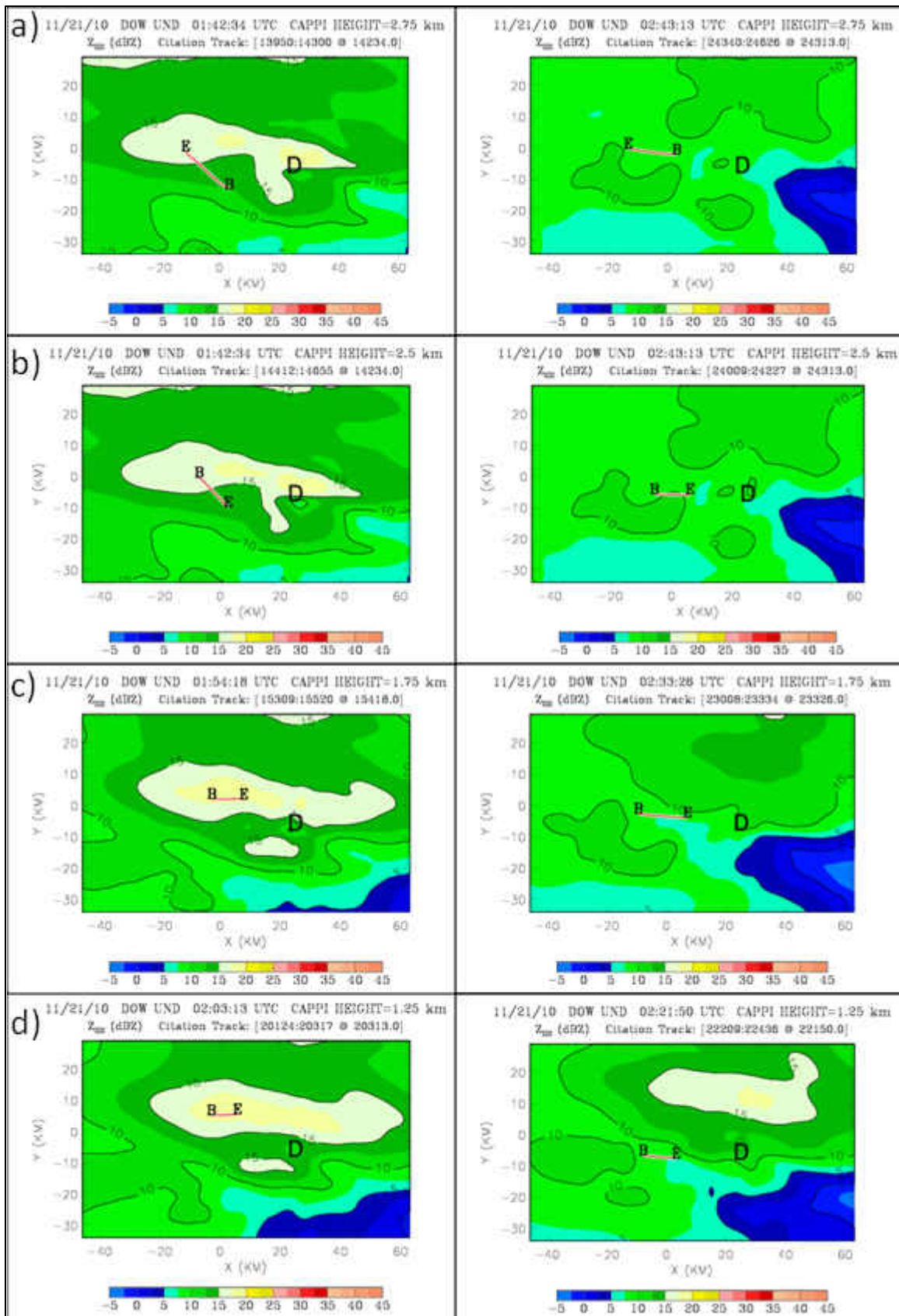


Fig. 11 cont.

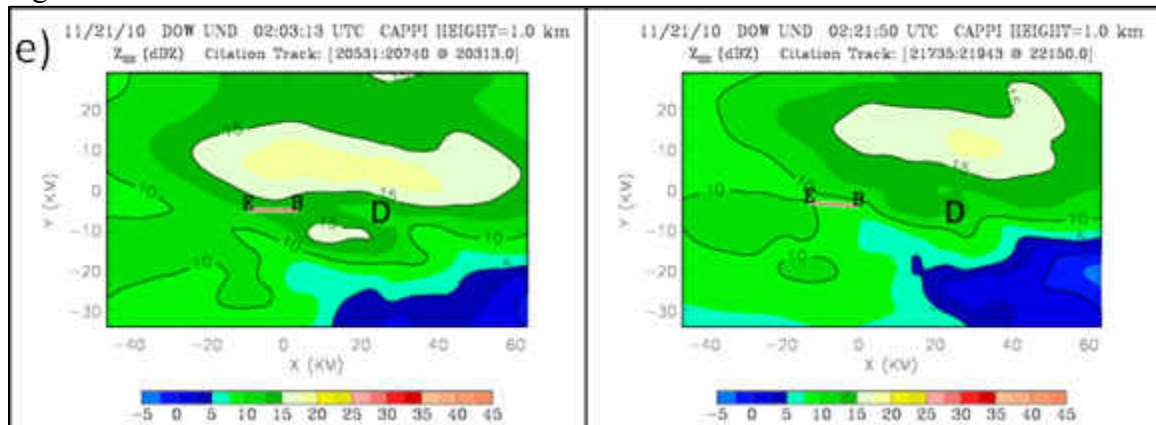


Fig. 11. Citation Research Aircraft transects inside and outside of the snowband overlaid with DOW reflectivity at (a) 2.75 km AGL, (b) 2.50 km, (c) 1.75 km, (d) 1.25 km, and (e) 1.00 km. The red lines indicate aircraft transects. The ‘B’ indicates aircraft transect start and the ‘E’ indicates transect end. Location of the DOW radar (D) is also shown.

First Transect-pair: 2.71 km AGL

For the first transect-pair, snow both inside and outside a snowband is sampled at approximately 2.71 km AGL (Fig. 11a). Using CAPPI images with aircraft transects, vertical velocities, and reflectivity contours, the area surrounding and west of the aircraft transect contains upward motion, while the area east of the transect contains mostly downward motion with small areas of upward motion (Fig. 12a). Vertical motion cannot be accurately determined within and near the baseline, which is the area without vertical velocity measurements extending to the northwest of the DOW location. However, after the snowband propagated out of the region, the vertical velocity values do not change much even though the reflectivity values decrease below those required to satisfy snowband criteria (Fig. 12b).

Inside the snowband the maximum reflectivity is between 15 – 17.5 dBZ with vertical velocity values along the aircraft transect increasing from 0 – 0.5 m s⁻¹ at the transect beginning to 1.5 – 2 m s⁻¹ at the transect end (Fig. 13a). Outside, the maximum reflectivity is

10 – 12.5 dBZ with vertical velocity values roughly the same as those inside the snowband (Fig. 13b). Despite the differences in reflectivity inside versus outside the snowband, the two kinematic fields are similar. Inside the snowband winds are generally easterly between 0.5 – 3.5 km and westerly between 6 – 9 km, and an updraft is present between 3.5 – 6 km (Fig. 14a). The overall kinematic pattern outside the snowband is very similar, with the updraft at roughly the same altitude (between 3 – 5 km; Fig. 14b).

Two slices perpendicular to the snowband long axis are used to compare the reflectivity and wind fields along multiple sections through the snowband. Slice length is larger than the band axis to include wind patterns through and around the snowbands. Since the stronger reflectivities in the northern part of the snowband are not within the dual-Doppler field, focus will remain on the reflectivities more towards the center of the plot. The slice on the far left side of the snowband (Fig. 15a) shows reflectivities of 12.5 – 17.5 dBZ in the center of the slice up to 7 km. A strong updraft tilted slightly towards the south is present throughout most of the slice. For the next slice to the right (Fig. 15b), reflectivities of 12.5 – 20 dBZ only extend upward to about 5.5 km. Again an updraft is present throughout the slice but with only a gradual southward tilt that is apparent above 4 km.

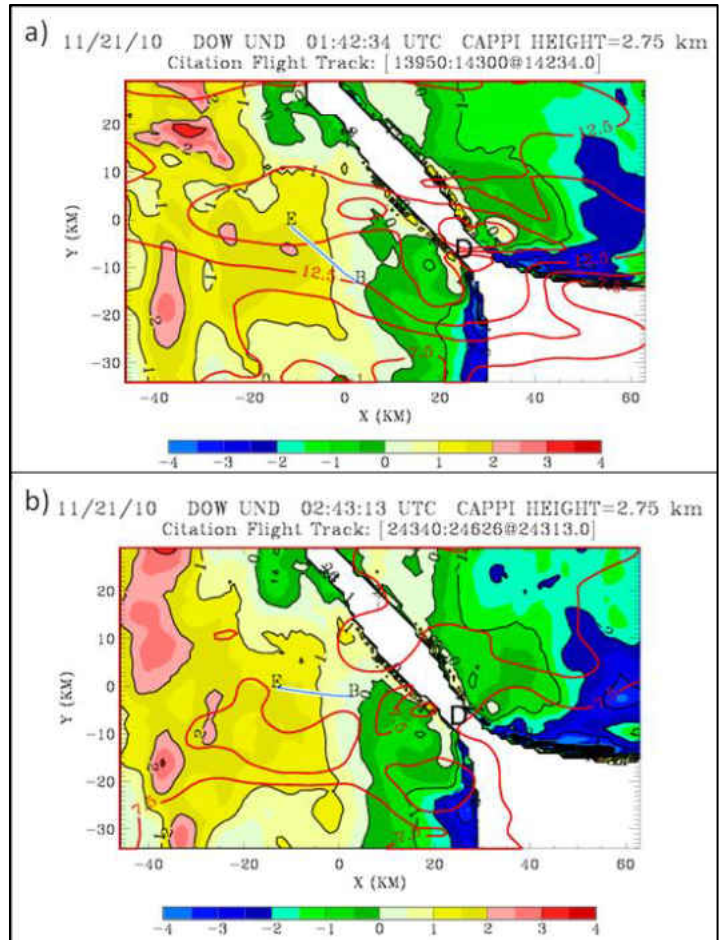


Fig. 12. Plots of vertical velocity at 2.75 km AGL overlaid with the locations of the Citation Research Aircraft flight transects (blue lines) inside (a) and outside the snowband (b). The 'B' indicates the aircraft transect beginning and the 'E' indicates the transect end. The red contours are reflectivity every 2.5 dBZ.

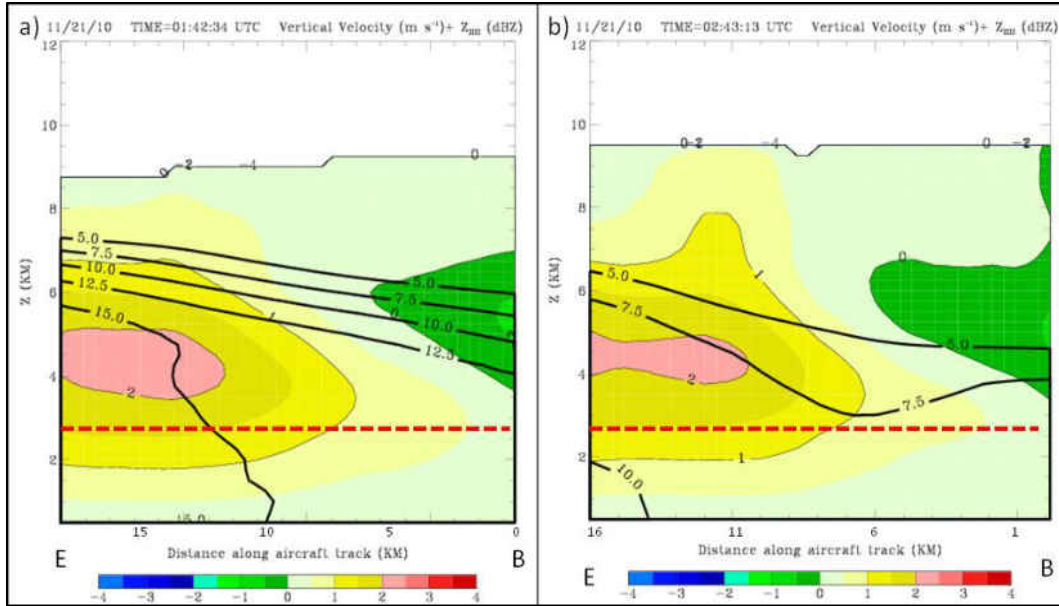


Fig. 13. Plots of vertical velocity overlaid with black contours of reflectivity along the aircraft transect in (a) and outside of (b) the snowband for the first transect-pair. The red dashed lines indicate Citation Research Aircraft flight transects. The ‘B’ indicates aircraft transect start and the ‘E’ indicates transect end. The Z axis starts at 0.5 km AGL.

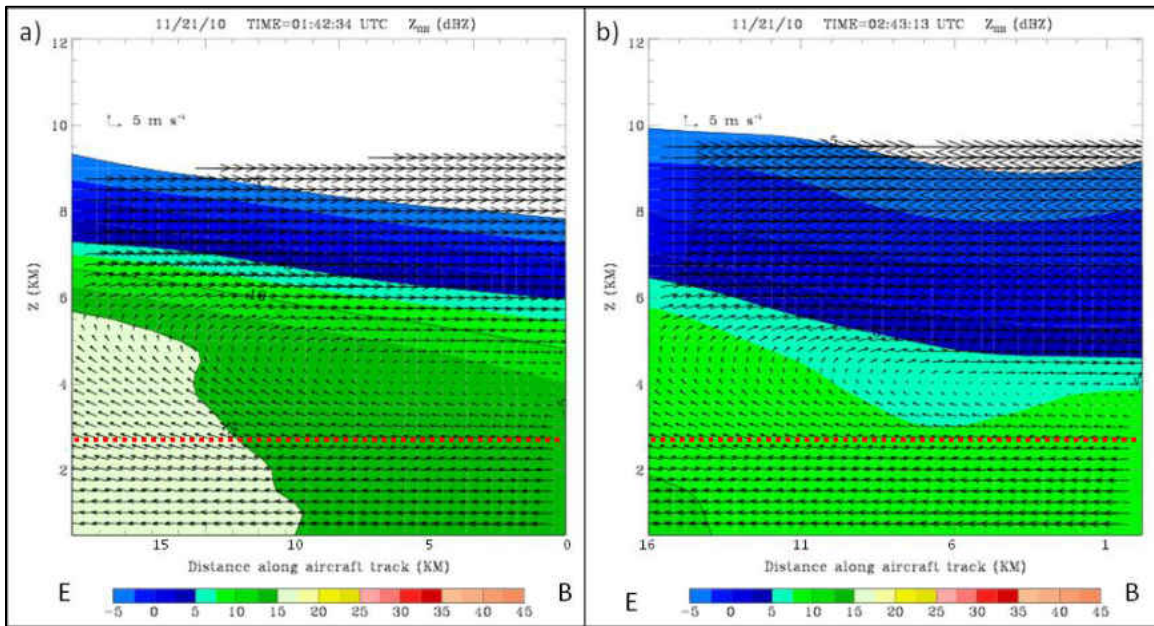


Fig. 14. Radar reflectivity cross sections along the aircraft transect inside (a) and outside (b) the snowband for the first transect-pair. Vectors indicate the wind in the plane of the cross section. The red dashed lines indicate the locations of the Citation Research Aircraft flight transects. The ‘B’ indicates the aircraft transect start and the ‘E’ indicates the transect end. Reference vectors in the horizontal and vertical direction along with a reference magnitude are provided in the upper left portion of each plot.

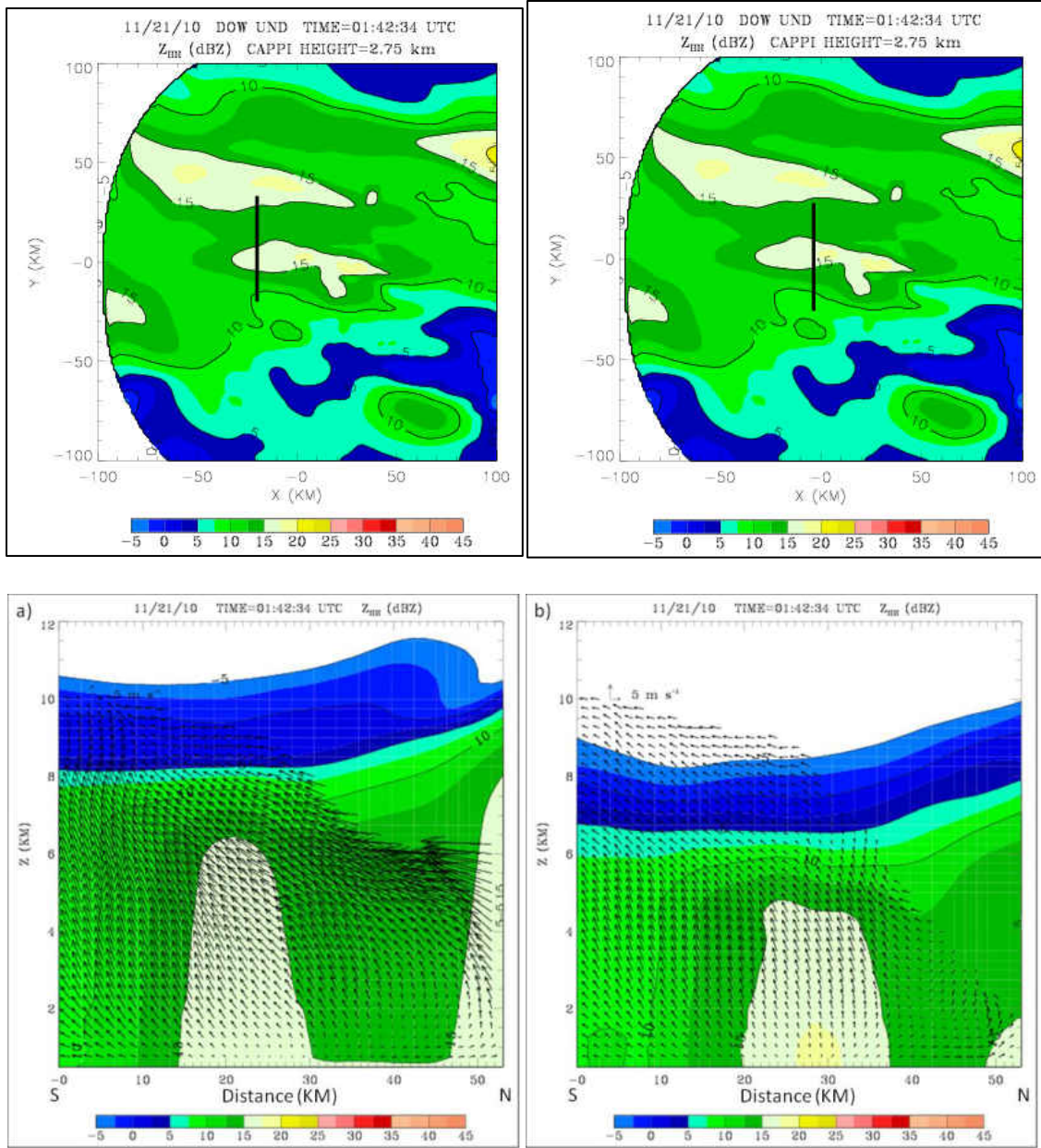


Fig. 15. Radar reflectivity slices with wind vectors at 2.75 km AGL. The CAPPI image above each slice shows the location of each image slice relative to the snowband. ‘S’ and ‘N’ indicate south and north. In each slice, horizontal and vertical reference vectors along with a reference magnitude are provided in the upper left portion of each plot.

Second Transect-pair: 2.41 km AGL

For the second transect-pair at an altitude of 2.41 km (Fig. 11b), the associated transect remained, temporally, within the same radar analyses as the transects from the previous pair. Thus the multi-Doppler fields used in the first transect-pair applies to the second transect-pair. The aircraft transect is in an area of upward motion inside the snowband, while outside the snowband the aircraft progresses from upward motion at the transect start to downward motion at the transect end (Fig. 16). Slices inside the snowband (Fig. 17a) along the aircraft transect show decreasing vertical velocity values from $1 - 1.5 \text{ m s}^{-1}$ at the transect beginning to $0 - 0.5 \text{ m s}^{-1}$ at the transect end with maximum reflectivity values between $15 - 17.5 \text{ dBZ}$. Outside (Fig. 17b) the vertical velocity motion also decreases along the transect starting with $1 - 1.5 \text{ m s}^{-1}$ and ending with $-0.5 - 0 \text{ m s}^{-1}$. The maximum reflectivity outside the snowband is $10 - 12.5 \text{ dBZ}$. Again the kinematic fields are similar with those associated with the first transect-pair. Easterly winds are present inside the snowband between $0.5 - 3 \text{ km}$, westerly between $5.5 - 9.5 \text{ km}$, and an updraft is present between $3 - 5.5 \text{ km}$ (Fig. 18a). Outside the snowband the updraft is between $3.5 - 4.5 \text{ km}$, with easterly winds below 3.5 km and westerly above 4.5 km (Fig. 18b). Since both transects in this transect-pair remained within the same radar analyses as the previous transect-pair, multiple slices through the snowband are the same as those for the first pair (Fig. 15).

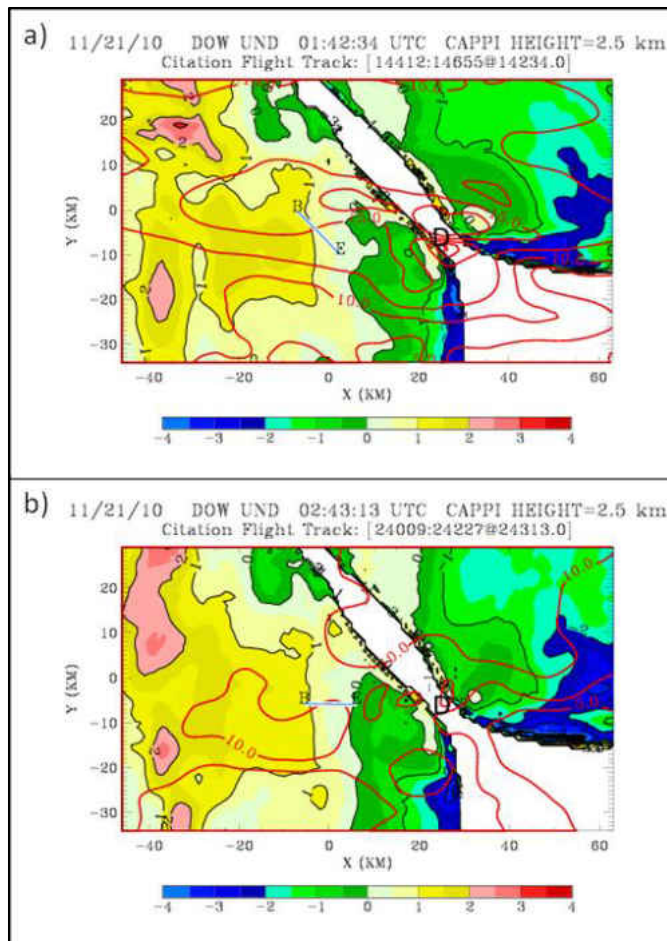


Fig. 16. Plots of vertical velocity at 2.5 km AGL overlaid with the locations of the Citation Research Aircraft flight transects (blue lines) inside (a) and outside the snowband (b). The 'B' indicates the aircraft transect beginning and the 'E' indicates the transect end. The red contours are reflectivity every 2.5 dBZ.

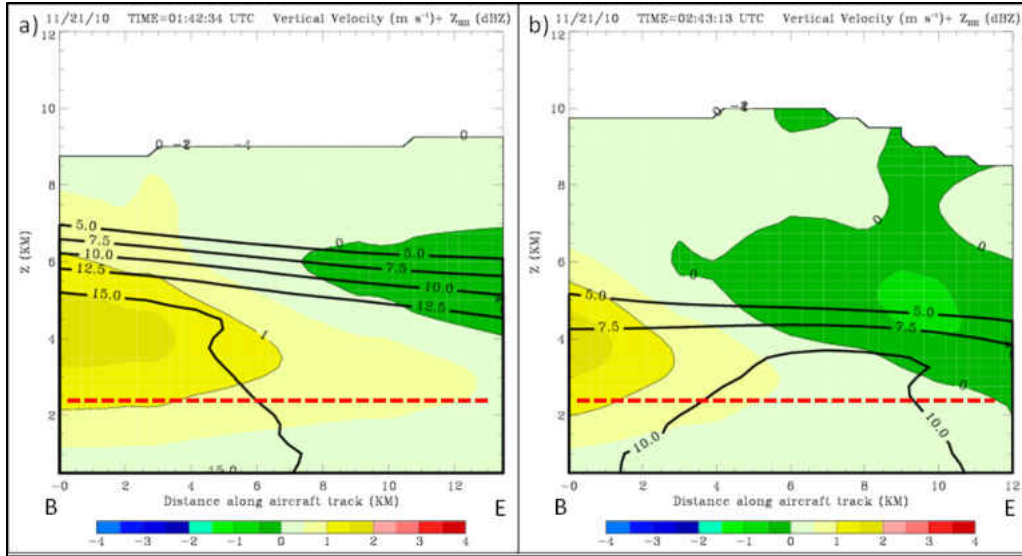


Fig. 17. Plots of vertical velocity overlaid with black contours of reflectivity along the aircraft transect in (a) and outside of (b) the snowband for the second transect-pair. The red dashed lines indicate locations of the Citation Research Aircraft flight transects. The ‘B’ indicates aircraft transect beginning and the ‘E’ indicates the transect end. The Z axis starts at 0.5 km AGL.

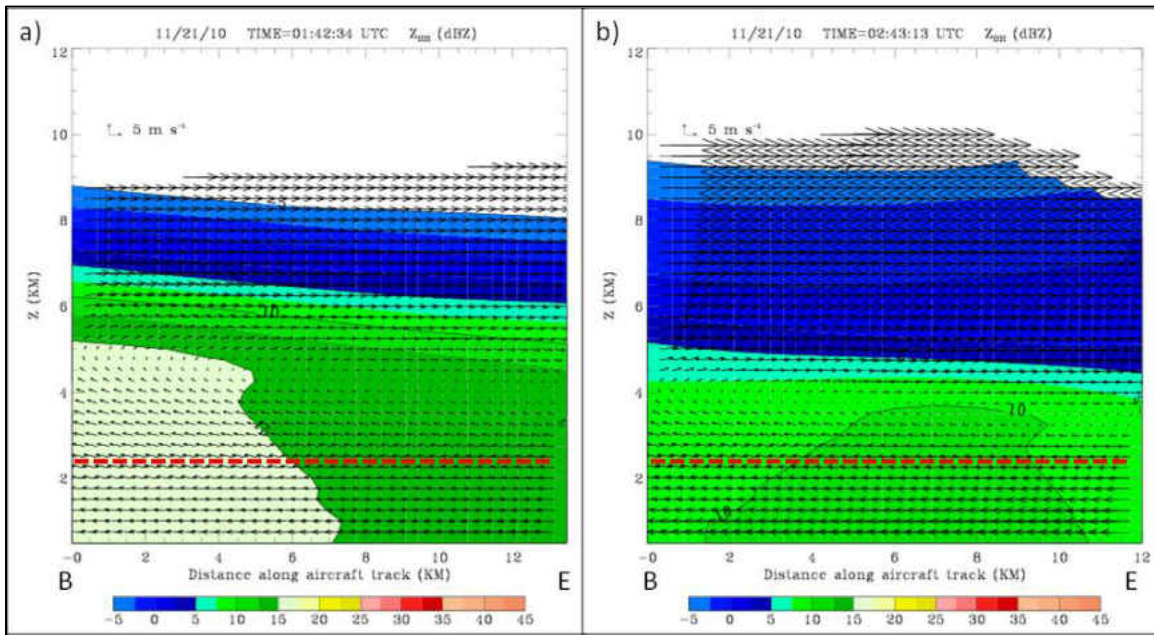


Fig. 18. Radar reflectivity cross sections along the aircraft transect inside (a) and outside (b) the snowband for the second transect-pair. Vectors indicate the wind in the plane of the cross section. The red dashed lines indicate locations of the Citation Research Aircraft flight transects. The ‘B’ indicates the aircraft transect start and the ‘E’ indicates the transect end. Reference vectors in the horizontal and vertical direction along with a reference magnitude are provided in the upper left portion of each plot.

Third Transect-pair: 1.80 km AGL

The third snowband transect-pair (Fig. 11c) contains similar vertical velocity characteristics to those associated with previous transect-pairs, however the aircraft transect inside the snowband is closer to the radar baseline than in the previous two transect-pairs. As with the second transect-pair, transects both inside and outside the snowband begin in an area of upward motion and end in downward motion (Fig. 19). Unlike the previous transect-pairs, vertical velocity inside the snowband along the transect has mostly negative values (most noticeably above 4 km), even when reflectivity has greater values inside than outside the snowband. Inside the snowband, the aircraft transect begins with vertical velocity values $0 - 0.5 \text{ m s}^{-1}$ before decreasing about half way along the transect to -0.5 to 0 m s^{-1} ; all while reflectivity is between $15 - 20 \text{ dBZ}$ (Fig. 20a). Outside, the aircraft starts in values of $0.5 - 1 \text{ m s}^{-1}$ which decrease to -0.5 to 0 m s^{-1} all while reflectivity is between $5 - 10 \text{ dBZ}$ (Fig. 20b). Accounting for the bias explained at the beginning of the chapter between the aircraft and radar data could strongly impact the vertical velocity for this transect-pair. Adding 1 m s^{-1} to the dual-Doppler retrieved vertical velocity values along the transect inside the snowband would change the magnitude along the transect from negative values in the later half of the transect to positive values. The vertical velocity along the transect would change to upward motion along the entire transect instead of both upward and downward motion.

When comparing slices of reflectivity and wind vectors for this transect-pair, reflectivity values and wind vector directions are similar to those associated with previous transect-pairs. Inside, both reflectivity contours and the wind directional shift descend in altitude along the aircraft transect (Fig. 21a). The weakest winds usually coincide near the 15 dBZ reflectivity contour. Outside, a circulation is detectable above the aircraft transect

with areas of upward motion near the aircraft transect beginning between 3.75 – 4.25 km, and downward motion near the aircraft transect end between 2.75 – 4 km. The wind shift also descends slightly with altitude along the transect (Fig. 21b).

The western slice taken perpendicular to the snowband long axis (Fig. 22a) shows reflectivities in the center of the slice between 12.5 – 20 dBZ extending up to 5.5 km. As with the first two transect-pairs, this slice has an updraft that is tilted towards the south. Beyond 30 km along the slice the winds shift direction, coming from the south instead of the north. For the eastern slice (Fig. 22b), downward motion is present even in areas of reflectivity between 12.5 – 17.5 dBZ. The downward motion does have some variability depending on height. Between 0.5 – 2 km there is a wind component coming from the south, and above 4 km there is a component coming from the north.

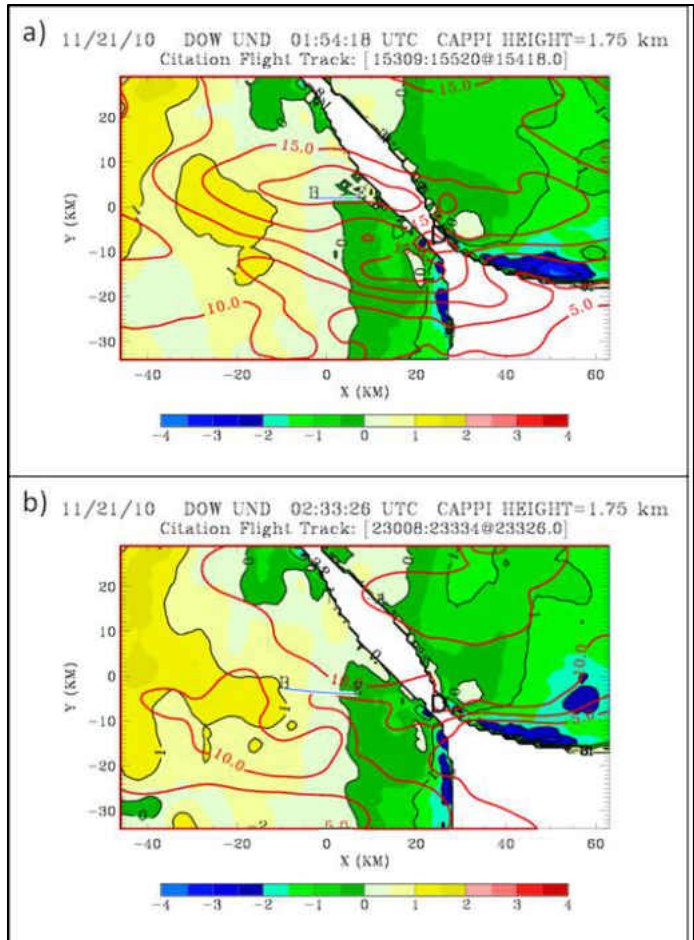


Fig. 19. Plots of vertical velocity at 1.75 km AGL overlaid with the locations of the Citation Research Aircraft flight transects (blue lines) inside (a) and outside the snowband (b). The 'B' indicates the aircraft transect beginning and the 'E' indicates the transect end. The red contours are reflectivity every 2.5 dBZ.

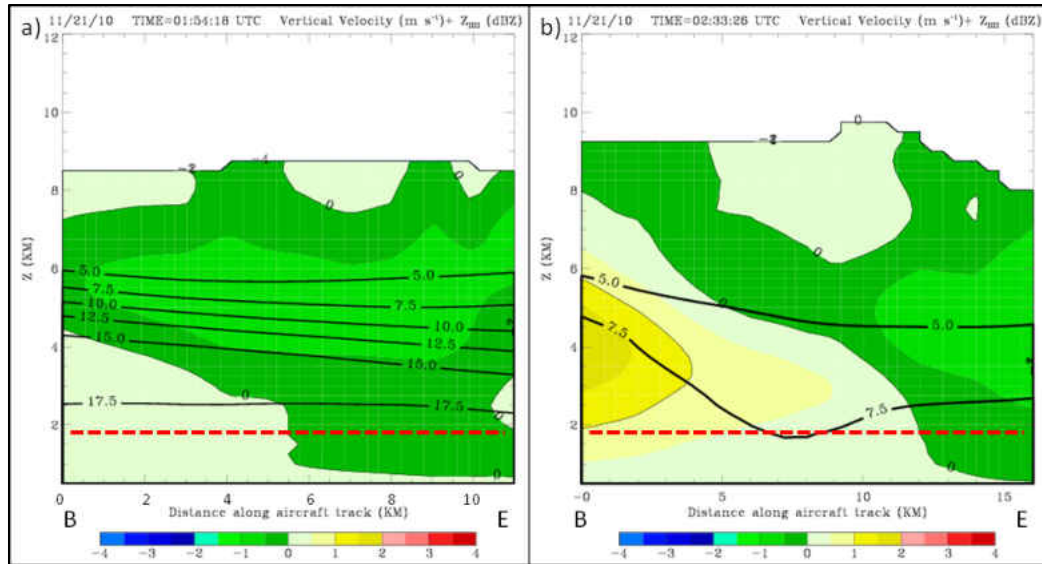


Fig. 20. Plots of vertical velocity overlaid with black contours of reflectivity along the aircraft transect in (a) and outside of (b) the snowband for the third transect-pair. The red dashed lines indicate locations of the Citation Research Aircraft flight transects. The ‘B’ indicates aircraft transect beginning and the ‘E’ indicates the transect end. The Z axis starts at 0.5 km AGL.

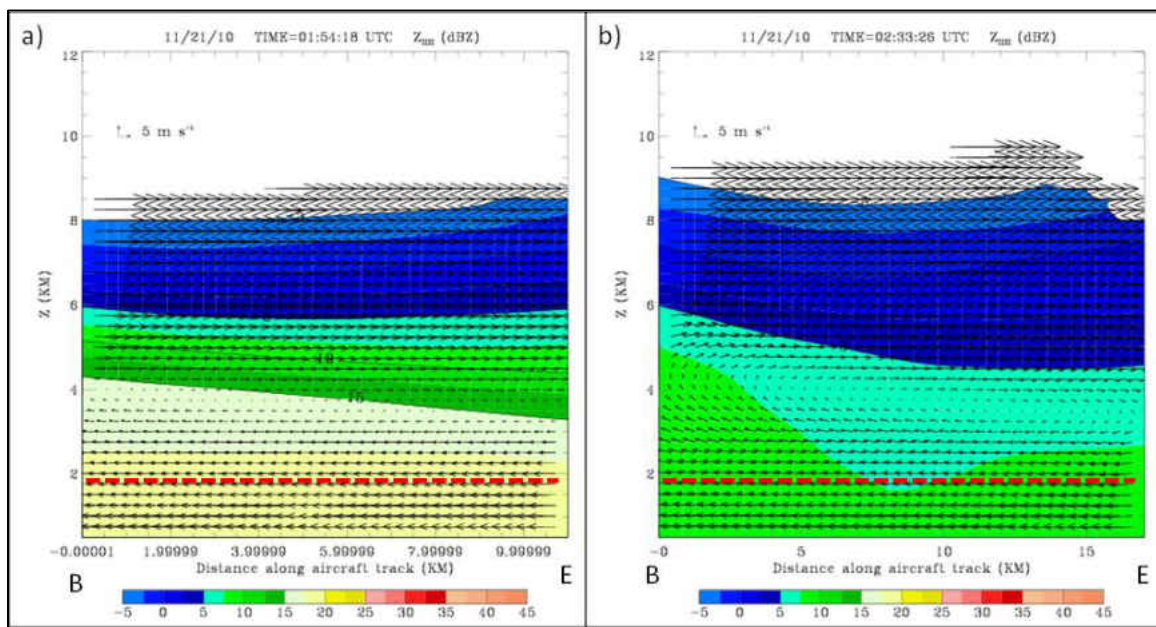


Fig. 21. Radar reflectivity cross sections along the aircraft transect inside (a) and outside (b) the snowband for the third transect-pair. Vectors indicate the wind in the plane of the cross section. The red dashed lines indicate the locations of the Citation Research Aircraft flight transects. The ‘B’ indicates the aircraft transect start and the ‘E’ indicates the transect end. Reference vectors in the horizontal and vertical direction along with a reference magnitude are provided in the upper left portion of each plot.

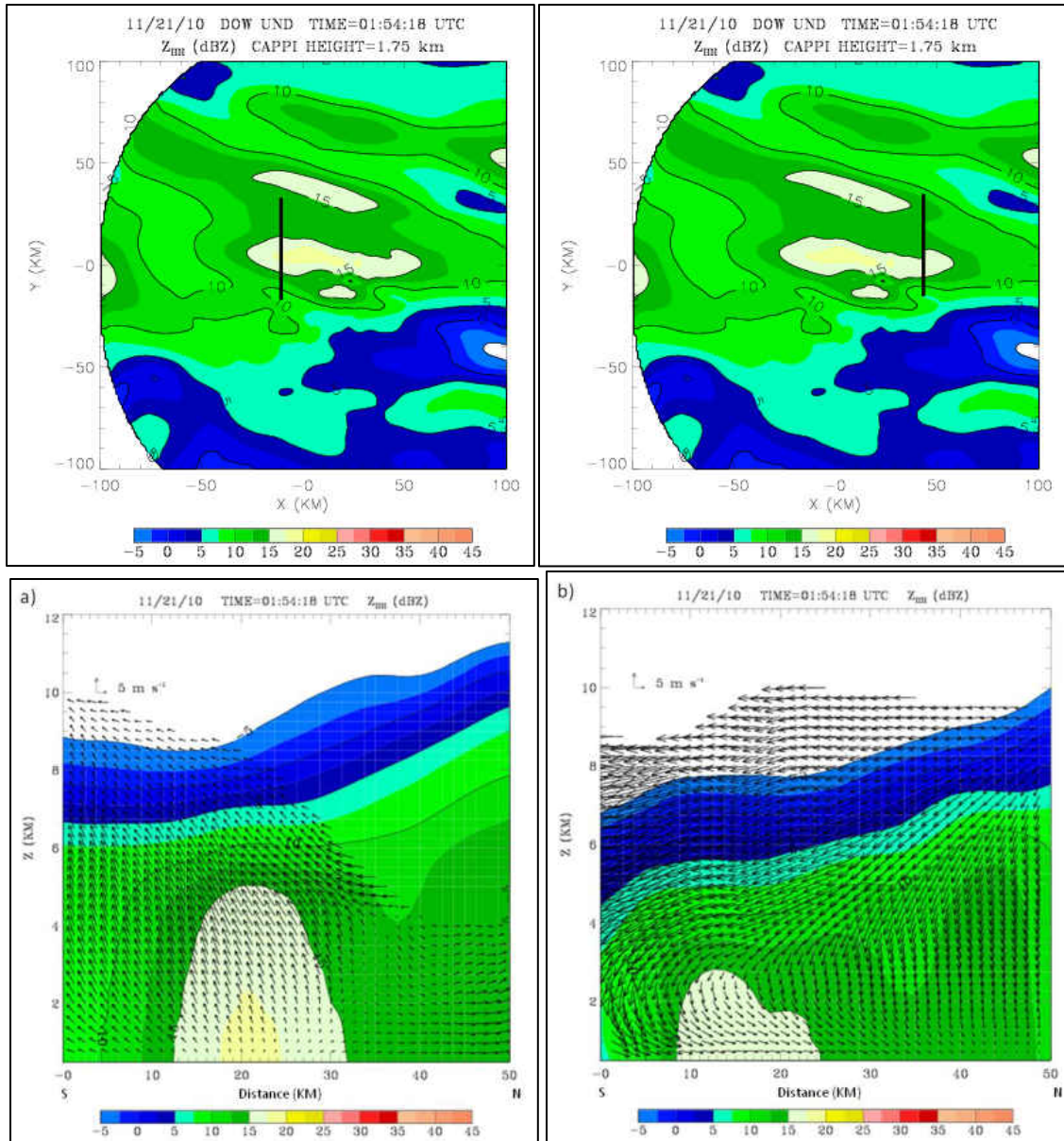


Fig. 22. Radar reflectivity slices with wind vectors at 1.75 km AGL. The CAPPI image above each slice shows the location of each image slice relative to the snowband. The ‘S’ and ‘N’ indicate south and north. In each slice, horizontal and vertical reference vectors along with a reference magnitude are provided in the upper left portion of each plot.

Fourth Transect-pair: 1.19 km AGL

For the fourth transect-pair (Fig. 11d) at an altitude of 1.19 km AGL, upward motion is most prominent in the western lobe (Fig. 23a). Areas of downward motion are mostly in the eastern lobe, along with some downward motion just to the west of the DOW location

(Fig. 23b). Again the aircraft transect inside the snowband is closer to the radar baseline than the first and second transect-pairs. Slices of vertical velocity with reflectivity contours through the aircraft transect are similar to the third transect-pair. The transect inside the snowband has vertical velocity values slightly above 0 m s^{-1} between $0 - 3.5 \text{ km}$, and negative vertical velocity values above 3.5 km (Fig. 24a), while outside the snowband the vertical velocity values along the aircraft transect gradually decrease over the flight transect (Fig. 24b). Higher reflectivity values inside the snowband are consistent with the previous transect-pairs. Accounting for the bias explained earlier between the aircraft and radar data would increase the retrieved vertical velocity along the transect inside the snowband from $0 - 0.5 \text{ m s}^{-1}$ to $1 - 1.5 \text{ m s}^{-1}$.

Slices of reflectivity values and wind vector directions are very similar to the third transect-pair both inside and outside the snowband. Inside the snowband the maximum reflectivity is between $17.5 - 20 \text{ dBZ}$ with easterly winds between $0.5 - 4 \text{ km}$ and westerly winds between $4 - 8 \text{ km}$ (Fig. 25a). Outside the snowband the maximum reflectivity is between $7.5 - 10 \text{ dBZ}$ with low level easterly winds, higher level westerly winds, and a wind shift around 4 km (Fig. 25b). The decrease in the altitude of the wind shift along the aircraft transects is also evident for this transect-pair.

Two slices through the snowband show characteristics similar to as those in the third transect-pair. For the western slice (Fig. 26a), snowband reflectivities vary between $12.5 - 20 \text{ dBZ}$ and extend up to 5 km , with the region of upward motion having a slight southward tilt. The eastern slice (Fig. 26b) has generally downward motion with wind components similar to those in the eastern slice for the third transect-pair between $0 - 2 \text{ km}$ and above 4 km (Fig. 22b).

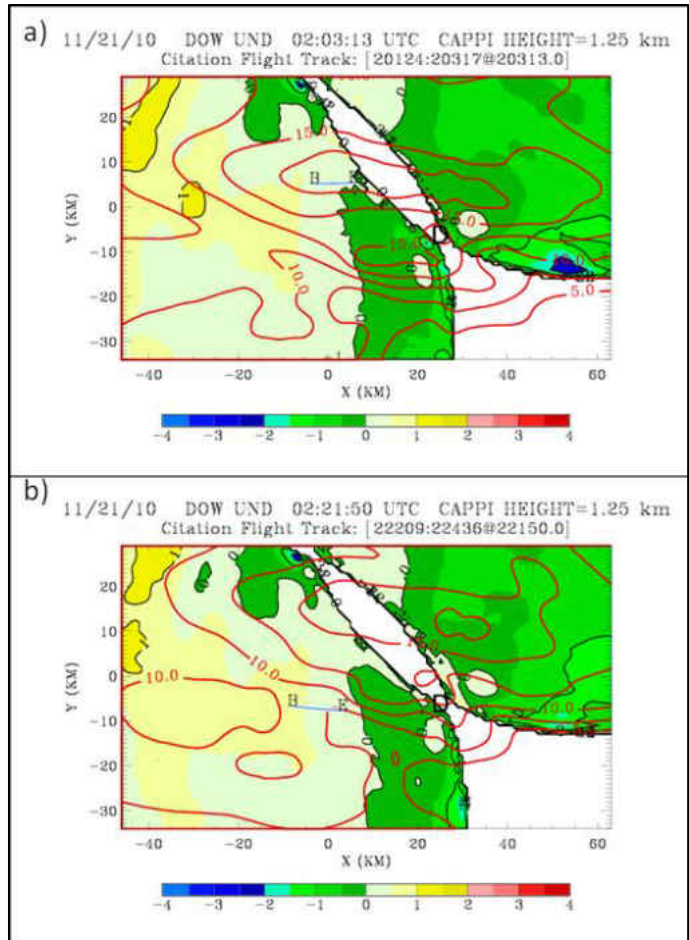


Fig. 23. Plots of vertical velocity at 1.25 km AGL overlaid with the locations of the Citation Research Aircraft flight transects (blue lines) inside (a) and outside the snowband (b). The 'B' indicates the aircraft transect beginning and the 'E' indicates the transect end. The red contours are reflectivity every 2.5 dBZ.

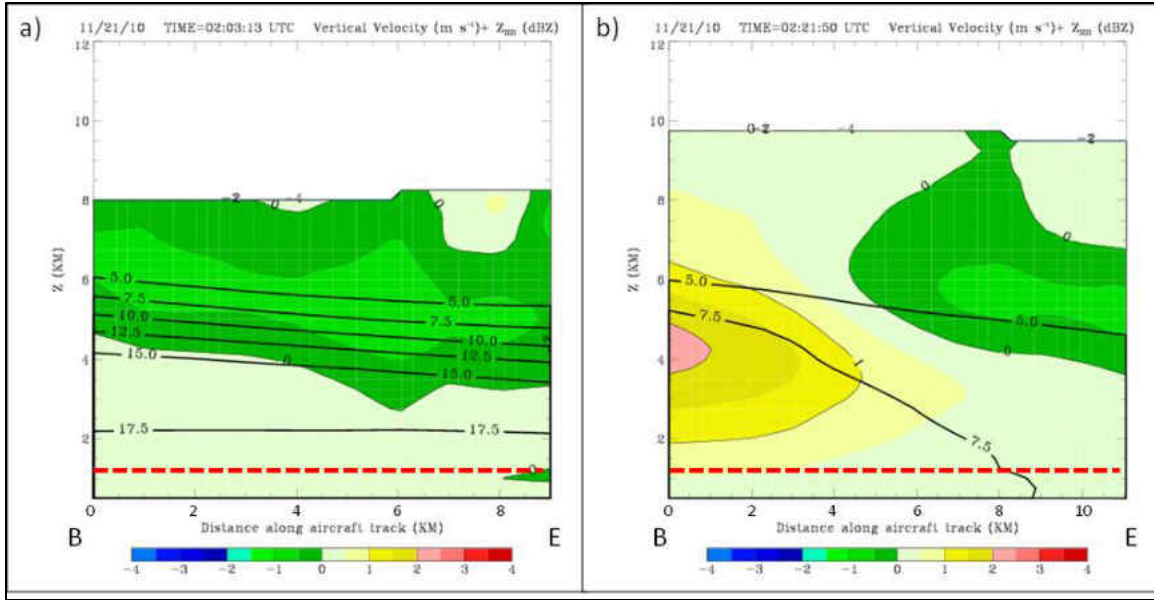


Fig. 24. Plots of vertical velocity overlaid with black contours of reflectivity along the aircraft transect in (a) and outside of (b) the snowband for the fourth transect-pair. The red dashed lines indicate locations of the Citation Research Aircraft flight transects. The ‘B’ indicates aircraft transect beginning and the ‘E’ indicates the transect end. The Z axis starts at 0.5 km AGL.

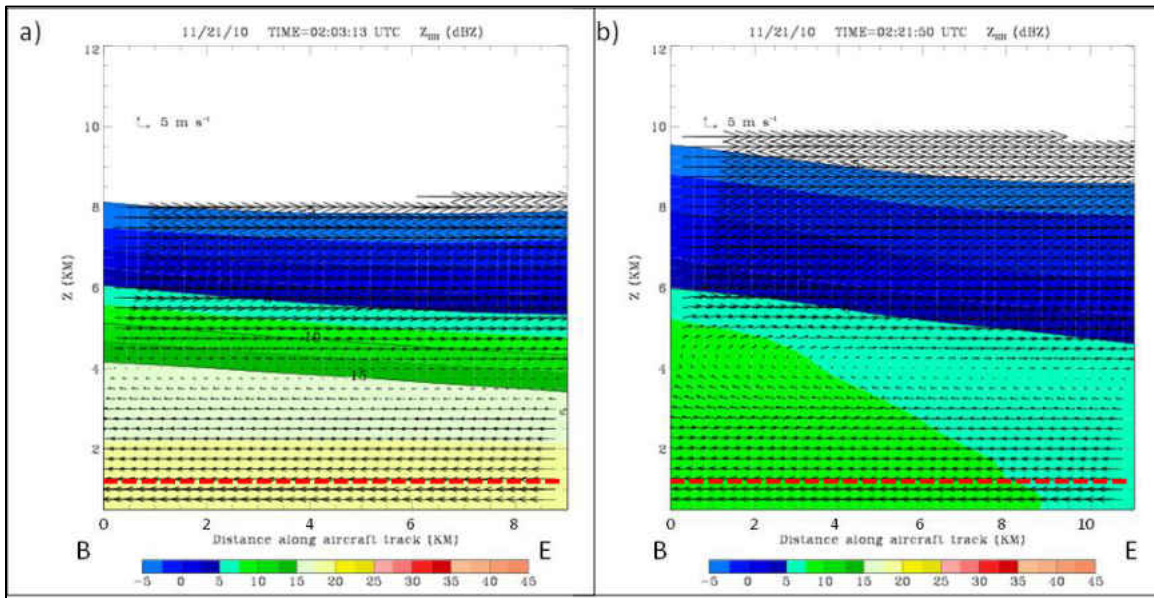


Fig. 25. Radar reflectivity cross sections along the aircraft transect inside (a) and outside (b) the snowband for the fourth transect-pair. Vectors indicate the wind in the plane of the cross section. The red dashed lines indicate locations of the Citation Research Aircraft flight transects. The ‘B’ indicates the aircraft transect start and the ‘E’ indicates the transect end. Reference vectors in the horizontal and vertical direction along with a reference magnitude are provided in the upper left portion of each plot.

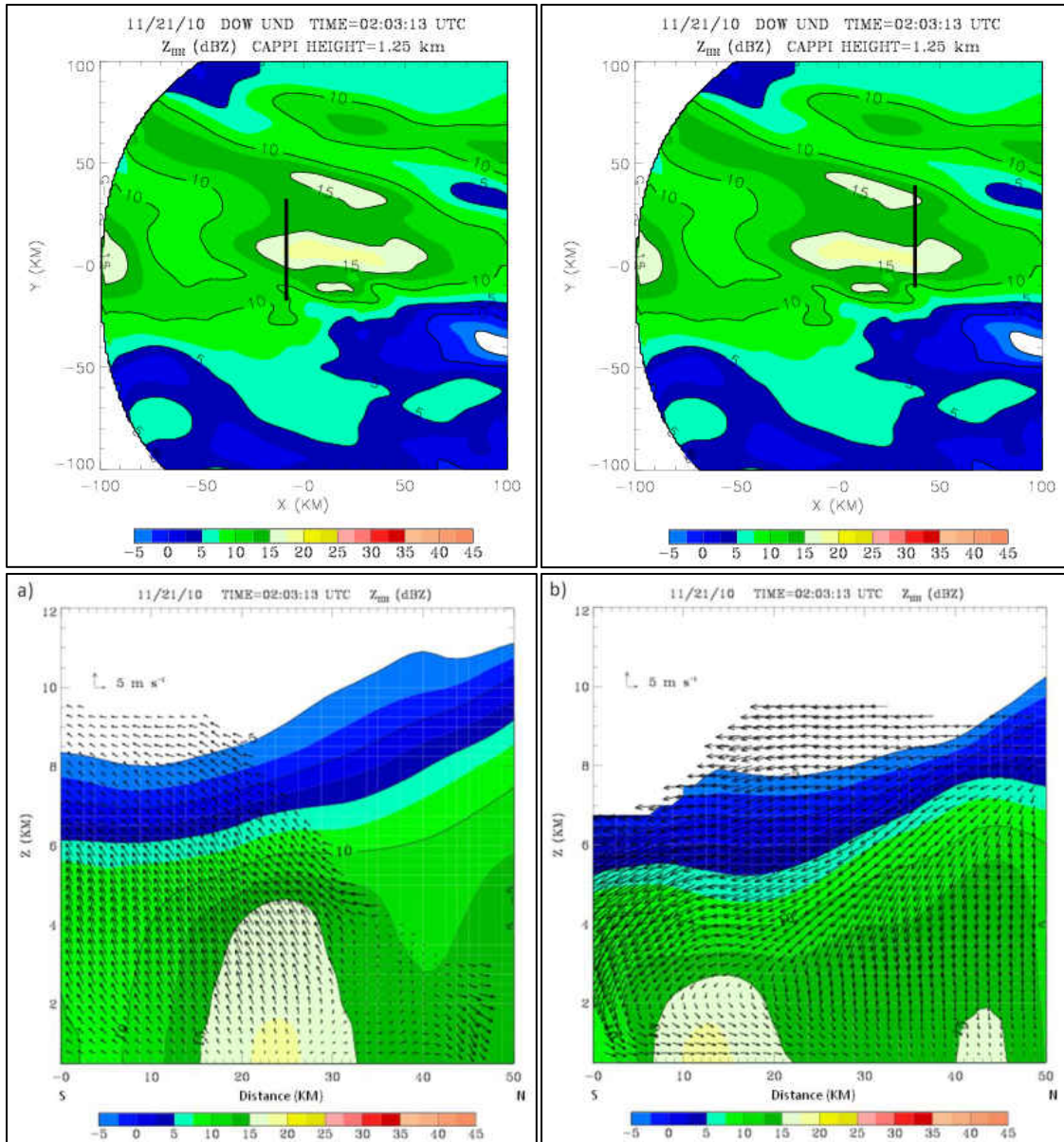


Fig. 26. Radar reflectivity slices with wind vectors at 1.25 km AGL. The CAPPI image above each slice shows the location of each image slice relative to the snowband. In the slice images, the red dashed line indicates the locations of the Citation Research Aircraft flight transect. The ‘S’ and ‘N’ indicate south and north. In each slice, horizontal and vertical reference vectors along with a reference magnitude are provided in the upper left portion of the plot.

Fifth Transect-pair: 0.89 km AGL

For the fifth transect-pair (Fig. 11e), the aircraft transect is just inside the southern edge of the snowband while still within the required 12.5 dBZ reflectivity value. Many of

the features from the first four transect-pairs are present in the fifth transect-pair. The western lobe contains upward motion along with some downward motion just to the west of the DOW location (Fig. 27a), and the eastern lobe had mostly downward motion (Fig. 27b). The vertical velocity values along both the inside and outside transects for this transect-pair are $0 - 0.5 \text{ m s}^{-1}$. The transect inside the snowband has a greater area of $10 - 15 \text{ dBZ}$ reflectivity (Fig. 28a). While both vertical slices along the aircraft transects inside and outside the snowband have negative velocity values at the beginning and positive values at the end, the negative (positive) values inside (outside) the snowband are stronger than those outside (inside). The transect outside the snowband has predominately positive velocity values above 1 km (Fig. 28b), unlike the velocity values for the transect inside the snowband. The kinematic patterns of both transects are similar to previous transect-pairs, with low level easterlies, upper level westerlies, and a directional wind shift from east-to-west with height (Fig. 29). Since both transects in this transect-pair remained within the same radar analyses as the transects from the previous transect-pair, multiple slices through the snowband are the same as in the fourth transect-pair (Fig. 26).

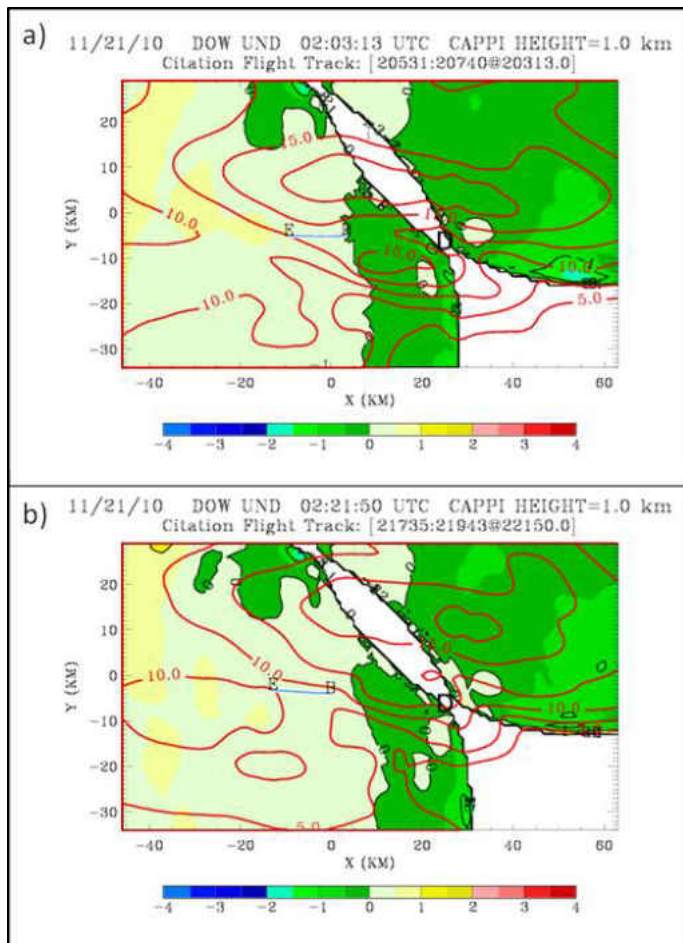


Fig. 27. Plots of vertical velocity at 1.0 km AGL overlaid with the locations of the Citation Research Aircraft flight transects (blue lines) inside (a) and outside the snowband (b). The 'B' indicates the aircraft transect beginning and the 'E' indicates the transect end. The red contours are reflectivity every 2.5 dBZ.

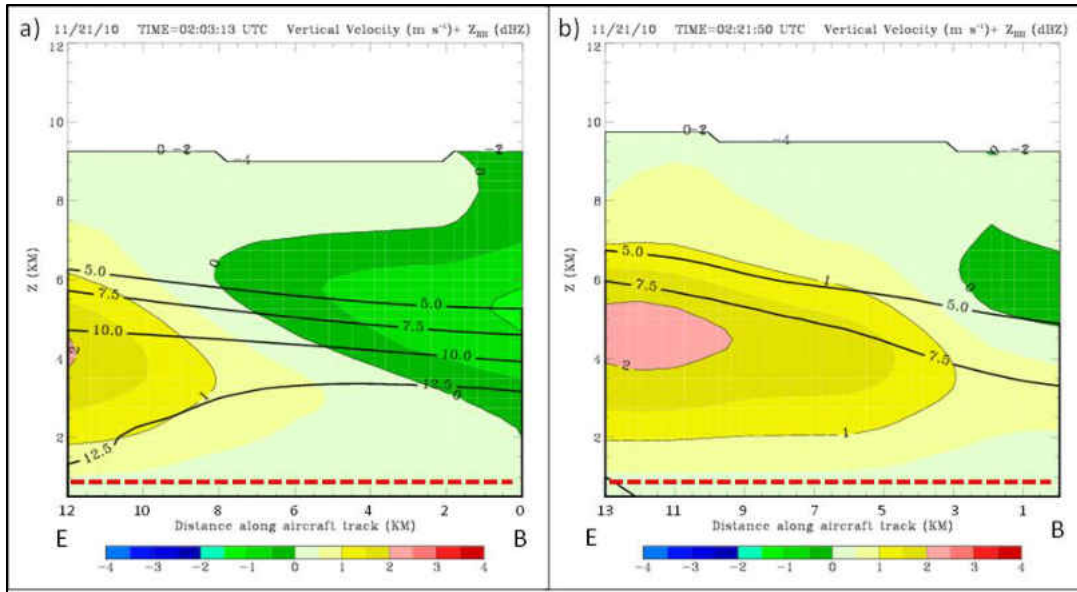


Fig. 28. Plots of vertical velocity overlaid with black contours of reflectivity along the aircraft transect in (a) and outside of (b) the snowband for the fifth transect-pair. The red dashed lines indicate locations of the Citation Research Aircraft flight transects. The ‘B’ indicates aircraft transect beginning and the ‘E’ indicates the transect end. The Z axis starts at 0.5 km AGL.

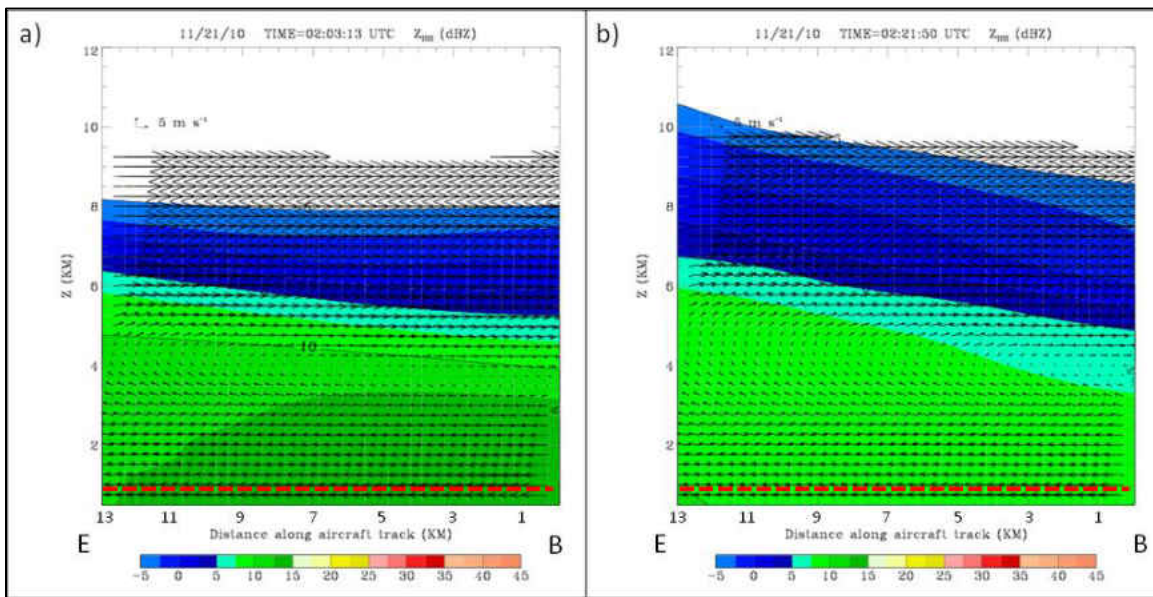


Fig. 29. Radar reflectivity cross sections along the aircraft transect inside (a) and outside (b) the snowband for the fifth transect-pair. Vectors indicate wind in the plane of the cross section. The red dashed lines indicate locations of the Citation Research Aircraft flight transects. The ‘B’ indicates the aircraft transect start and the ‘E’ indicates the transect end. Reference vectors in the horizontal and vertical direction along with a reference magnitude are provided in the upper left portion of each plot.

Radair-Aircraft Transect Analysis Results

Radair value trends along the aircraft transects both inside and outside the snowband are shown for both the DOW and UND radars in Fig. 30 and averages are shown in Tables 10 and 11. The plots for inside the snowband in Fig. 30 are truncated to restrict the aircraft transect to only the portion that was inside the snowband (from the definition discussed at the beginning of Chapter III).

For both the DOW and UND radars, the reflectivity values inside the snowband are greater than those outside for all five altitudes. For the DOW data, the Z_{DR} values inside the snowband are lower than those outside the snowband. However, the UND Z_{DR} values outside the snowband are lower than those inside the snowband, which is not consistent with the DOW data or with previous research. Radar calibration differences and noise within the radar data could be the reason the polarimetric UND data are different than the polarimetric DOW data. Specific differential phase values inside the snowband are more variable at higher altitudes than at lower altitudes. In Fig. 30a, the K_{DP} values towards the beginning of the transect are lower inside the snowband than outside. At the transect end, the inside values are higher. Figures 10c and 10d start with inside K_{DP} values being higher than outside, with this reversing by the end of the transect. For the rest, the inside values are either larger than the outside values (Fig. 10e – i), or both the inside and outside values are very similar (Fig. 10b, j). For both radars, values of ρ_{HV} inside the snowband are generally larger than values outside. There are a few exceptions wherein a segment of the outside values exceeds inside values (Fig. 10a) or both sets of ρ_{HV} values are equal (Fig. 10c).

Tables 10 and 11 provides average DOW and UND radar parameter values for each aircraft transect in addition to averages over all five altitudes both inside and outside of the

snowband. The average transect radar parameter values inside (outside) the snowband are, 16.00 dBZ (8.77 dBZ), 0.49 dB (0.75 dB), 0.04 ° km⁻¹ (0.01 ° km⁻¹), and 0.97 (0.96). The average radar parameters values for the UND radar (Table 11) for inside (outside) are 12.53 dBZ (4.92 dBZ), 0.93 dB (0.67 dB), 0.06 ° km⁻¹ (0.04 ° km⁻¹), and 0.93 (0.85).

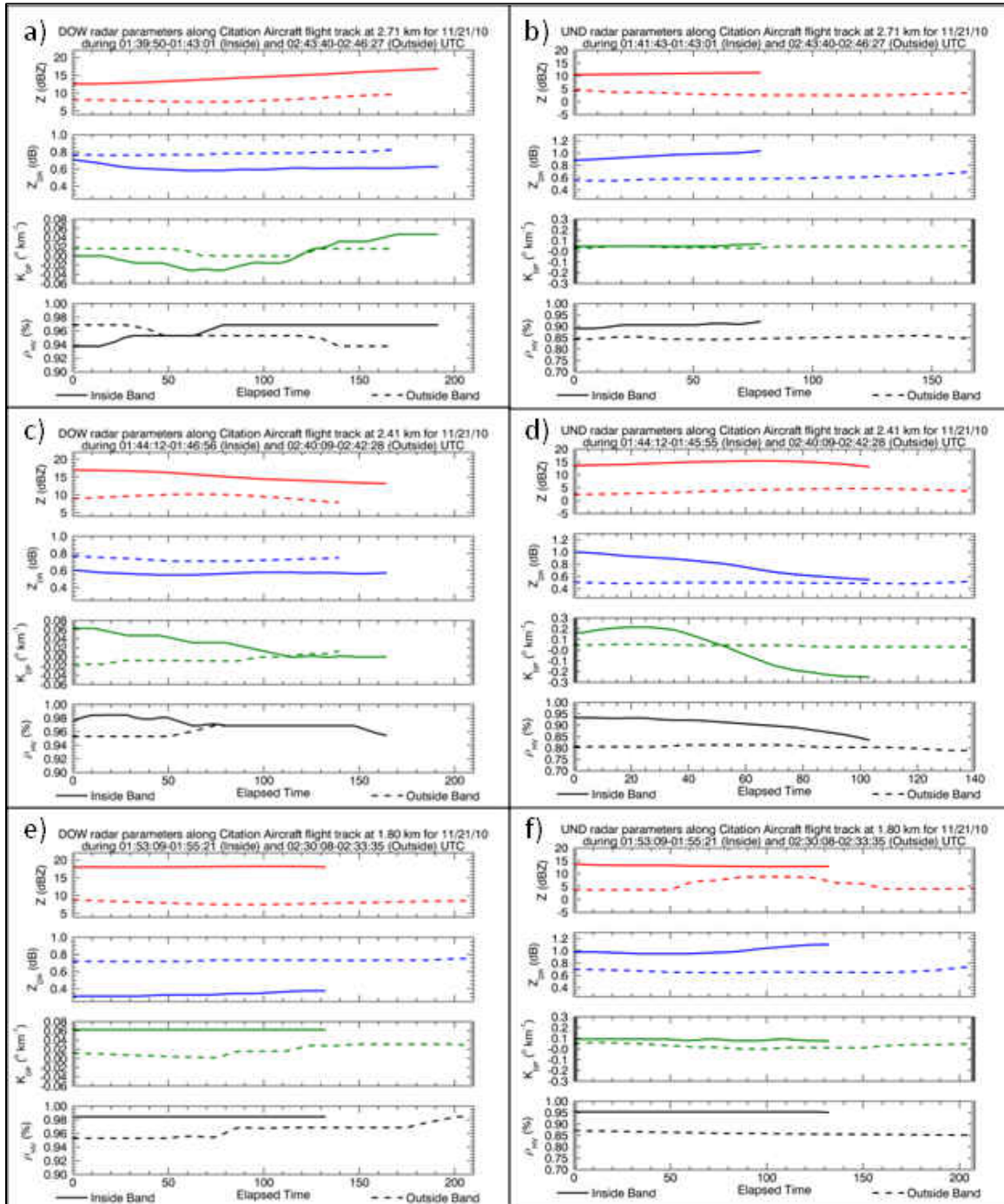


Fig. 30 cont.

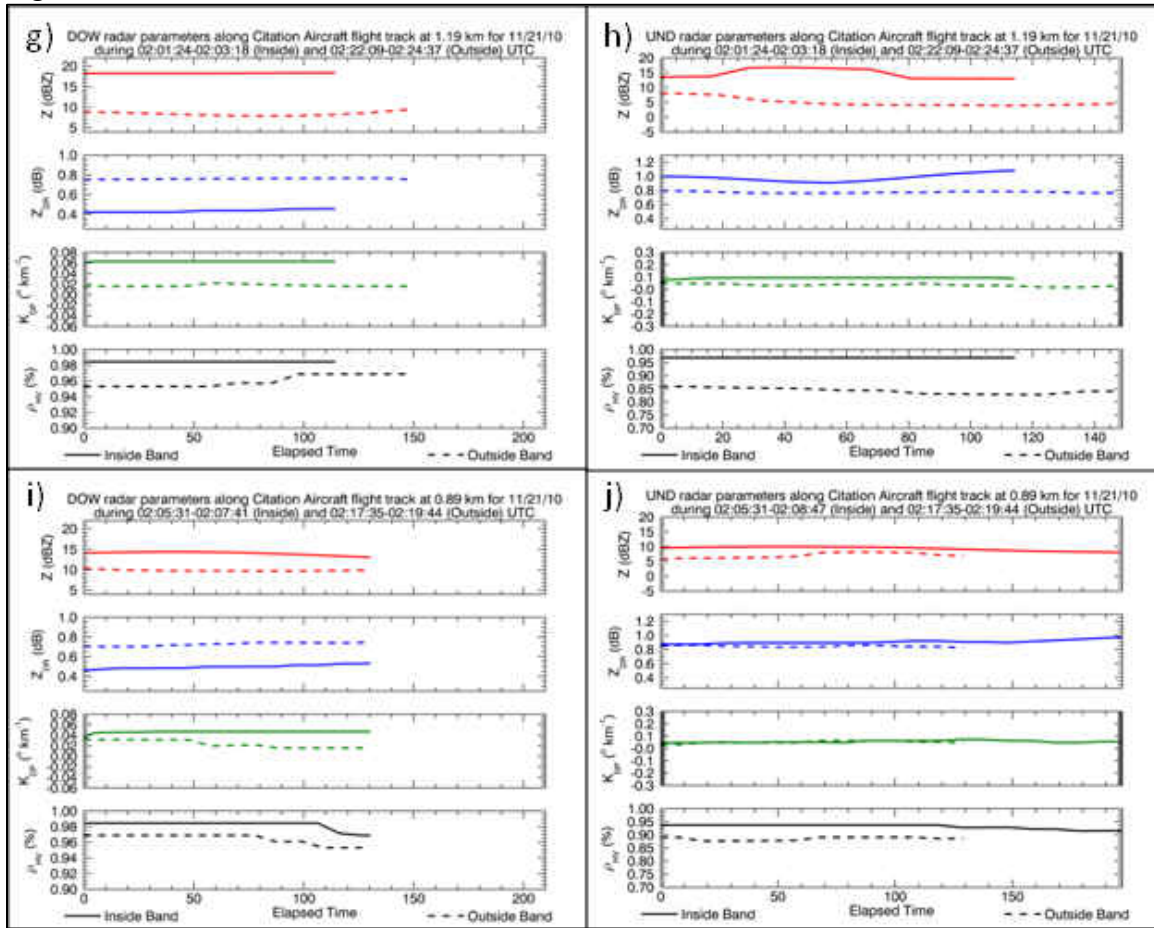


Fig. 30. Trends in DOW (a, c, e, g, i) and UND (b, d, f, h, j) reflectivity (red), differential reflectivity (blue), specific differential phase (green), and correlation coefficient (black) along the time-to-space corrected Citation Research Aircraft transects both inside (solid) and outside (dashed) the snowband. For the shown measurement periods at approximately (a – b) 2.71 km AGL, (c – d) 2.41 km AGL, (e – f) 1.80 km AGL, (g – h) 1.19 km AGL, and (i – j) 0.89 km AGL.

Table 10. Average values of Z , Z_{DR} , K_{DP} , and ρ_{HV} along each transect made by the Citation Research Aircraft both inside (In) and outside (Out) the snowband for the DOW radar, in addition to the column average.

DOW Radar								
Aircraft Height (nearest 0.01 km)	Z (dBZ)		Z _{DR} (dB)		K _{DP} (° km ⁻¹)		ρ _{HV}	
	In	Out	In	Out	In	Out	In	Out
2.71	14.51	8.20	0.61	0.78	0.003	0.01	0.96	0.95
2.41	15.15	9.46	0.57	0.73	0.03	-0.01	0.97	0.96
1.80	18.09	8.04	0.34	0.73	0.06	0.02	0.98	0.96
1.19	18.27	8.37	0.44	0.76	0.06	0.02	0.98	0.96
0.89	13.98	9.80	0.50	0.73	0.05	0.02	0.98	0.96
Average	16.00	8.77	0.49	0.75	0.04	0.01	0.97	0.96

Table 11. Average values of Z , Z_{DR} , K_{DP} , and ρ_{HV} along each transect made by the Citation Research Aircraft both inside (In) and outside (Out) the snowband for the UND radar, in addition to the column average.

UND Radar								
Aircraft Height (nearest 0.01 km)	Z (dBZ)		Z _{DR} (dB)		K _{DP} (° km ⁻¹)		ρ _{HV}	
	In	Out	In	Out	In	Out	In	Out
2.71	10.89	3.01	0.96	0.60	0.05	0.04	0.91	0.85
2.41	14.62	3.81	0.78	0.49	0.01	0.04	0.90	0.80
1.80	13.07	5.74	1.00	0.66	0.09	0.03	0.95	0.86
1.19	14.71	4.97	0.98	0.77	0.09	0.03	0.97	0.84
0.89	9.34	7.06	0.91	0.85	0.06	0.05	0.93	0.88
Average	12.53	4.92	0.93	0.67	0.06	0.04	0.93	0.85

Aircraft and Radar Analysis Through Snowband Core and Edge

Aircraft transects analyzed inside the snowband core are compared to transects through the snowband edge at the same height. The entire aircraft transect through a snowband (at a level altitude) is separated into smaller transects through the snowband edge and core (based on radar definition at the beginning of Chapter III). Using transects inside the snowband core and edge enable aircraft and radar comparisons of different snowband

sections that are much closer in time than previous methods. There were only two level transects where the aircraft flew through both the snowband edge and core. The first of these transects at an altitude of 2.71 km has an average vertical velocity of $1.7 \pm 0.2 \text{ m s}^{-1}$ in both the snowband edge and core. To analyze any differences in radar values between the two transect sections, the average reflectivity and Z_{DR} values in the snowband core are compared to those in the snowband edge. For the first transect, Table 12 summarizes the average reflectivity and Z_{DR} values in the snowband core and edge.

Table 12. Average reflectivity and Z_{DR} values from the first aircraft transect through the snowband core and edge at 2.71 km.

	Snowband Core	Snowband Edge
Average Reflectivity (dBZ)	14.51	12.62
Average Z_{DR} (dB)	0.61	0.73

For the second case, the aircraft transect at a height of 0.89 km goes from the core to the edge. The average vertical velocity in the snowband edge is $1.7 \pm 0.5 \text{ m s}^{-1}$, while in the core it is $1.7 \pm 0.3 \text{ m s}^{-1}$. Reflectivity and Z_{DR} values in the core and edge have similar patterns to those in the first case (Table 13).

Table 13. Average reflectivity and Z_{DR} values from the second aircraft transect through the snowband core and edge at 0.89 km.

	Snowband Core	Snowband Edge
Average Reflectivity (dBZ)	13.98	13.07
Average Z_{DR} (dB)	0.50	0.54

CHAPTER IV

DISCUSSION

Snowbands, defined earlier as elliptically-shaped regions having reflectivities at least 3 dB greater than surrounding values and lasting for at least two hours, are sampled using multiple dual-polarimetric radars and instrumented aircraft. The snowband sampled in this study did not occur in the northwest quadrant of an extratropical cyclone, and at times multiple snowbands that met the criteria outlined at the beginning of Chapter III existed. Aircraft measurements of hydrometeor size and number concentration, polarimetric radar parameters, and dual-Doppler wind retrievals are used to compare snowband properties to the non-banded snow regions, which are sampled after the snowband passed through the region. While kinematic characteristics of snowbands have been studied in prior research, how polarimetric radar variables relate to aircraft *in situ* data is lacking. Topics in this chapter include a review of the previous findings, how these findings compare with previous studies, and project limitations.

Summary of Results

As described in detail in the Chapter III, the 2DC probe images show that larger hydrometeors (900 – 2800 μm diameter) are more numerous inside the snowband, and smaller hydrometeors (300 – 900 μm) are more numerous outside the

snowband¹. (It is noted that “outside” refers to a precipitation region sampled well after the snowband had passed and not to an area immediately adjacent to the snowband.) While larger hydrometeors are sampled inside the snowband at all five sampled altitudes, concentrations of hydrometeors above $\sim 1000 \mu\text{m}$ change for all five altitudes both inside and outside the snowband. Concentrations of larger hydrometeors inside (outside) the snowband decrease (increase) with decreasing altitude. The size and concentration distributions inside and outside the snowband are more similar at the lowest sampled altitude than at higher altitudes.

At each altitude, inside and outside average aircraft-measured temperatures and vertical velocities are similar to each other. The average temperature inside (outside) the snowband is $-10.5 \text{ }^\circ\text{C}$ ($-10.7 \text{ }^\circ\text{C}$), and the average vertical velocity for both inside and outside is 1.6 m s^{-1} . Dual-Doppler retrieved vertical velocities along the aircraft path are not significantly different inside the snowband compared to outside at each of the five sampled altitudes. However, when examining wind vectors within image slices perpendicular to the snowband’s long axis, upward (downward) motion is generally in the western (eastern) lobe. For horizontal flow both inside and outside the snowband, the dual-Doppler retrieved wind direction changes from easterly at lower altitudes to westerly at higher altitudes, consistent with a 00 UTC Bismarck, ND sounding.

The average value for each polarimetric radar parameter (Z_{DR} , K_{DP} , and ρ_{HV}) along the aircraft track was compared inside and outside the snowband for both the UND and DOW radars. For both radars, by definition, reflectivity is greater inside the snowband (UND average of 12.53 dBZ, DOW average of 16.00 dBZ) compared to outside (UND

¹ An earlier study using this same dataset by Robak et al. (2012) found a consistent result: greater number concentrations between 2150 – 2800 μm inside and greater concentrations between 300 – 2150 μm outside the snowband.

average of 4.92 dBZ, DOW average of 8.77 dBZ). In addition, DOW reflectivity values both inside and outside are greater than the UND reflectivity values. Average DOW Z_{DR} values are greater outside the snowband, while average UND Z_{DR} values are greater inside the snowband. For both radars, average K_{DP} values are larger inside the snowband for most altitudes. Average ρ_{HV} values for both the DOW and UND radars are larger inside the snowband for all five altitudes. Average UND ρ_{HV} values outside the snowband are smaller than those obtained with the DOW.

Comparisons with Previous Literature

A cross section through a snowband from Kawashima and Fujiyoshi (2005) showed the strongest reflectivity values collocated with the strongest midlevel (~1.5 km AGL) upward motion, which was located above an area of low-level convergence. Areas of weaker reflectivity were located within weaker upward motion. However, other examples of snowband reflectivity and radial velocity from Steiger et al. (2013) showed the largest reflectivity values with the greatest vertical extent were displaced from the strongest low-level convergence regions. Thus, based upon two prior cases, it would seem that the updraft and reflectivity structure are case dependent. Herein, cross sections perpendicular to the snowband's long axis taken west of the DOW radar show upward motion predominantly located to the west of the DOW radar for each of the five transect-pairs, with kinematic fields similar to the snowband shown in Kawashima and Fujiyoshi (2005). Unique to this SNOWDUNDER case is that the snowband echo tops extended up to 9.5 km, higher than the ~3 km tops from Kawashima and Fujiyoshi (2005) and Steiger et al. (2013), and higher than the K-H wave tops (1.5 – 3 km AGL) from Houser and Bluestein (2011).

The hydrometeor concentration differences inside and outside the snowband for this study are similar to those observed by Robak et al. (2012) who analyzed one transect-pair from this case. Robak et al. (2012) identified greater concentrations between 2150 – 2800 μm inside the snowband, and greater concentrations between 300 – 2150 μm outside the snowband. While larger (smaller) hydrometeors have been identified inside (outside) the snowband in both this study and Robak et al. (2012), the hydrometeor size intervals inside and outside are different between the two studies.

Polarimetric radar values within snowbands are generally consistent with those observed in previous studies of aggregates. For all five transect-pairs, by definition, reflectivity is higher inside the snowband for both radars. Differential reflectivity is closer to 0 dB inside the snowband for the DOW radar, however this is not the case for the UND radar. Greater reflectivities and Z_{DR} values being closer to 0 dB in association with aggregated hydrometeors is consistent with previous research from airborne radar and *in situ* measurements (Meischner et al. 1991), observational and modeling studies of polarimetric variables (Straka et al. 2000), and polarimetric radar studies (May and Keenan 2005). However, these three studies did not focus exclusively on precipitation from snowbands.

Values for other polarization parameters are not entirely consistent with previous research. The average K_{DP} values for the DOW radar are 0.04 and 0.01 $^{\circ}\text{km}^{-1}$ for inside and outside the snowband, respectively. Average K_{DP} values for UND are 0.06 $^{\circ}\text{km}^{-1}$ inside and 0.04 $^{\circ}\text{km}^{-1}$ outside. Both the DOW and UND averages of K_{DP} are consistent with the K_{DP} values for dry and wet/aggregated snow as provided by Straka et al. (2000) and May and Keenan (2005), even though the values compiled by Straka et al. (2000) are for a 10 cm wavelength radar. However, for both the DOW and UND, K_{DP} inside the snowband is larger

than outside the snowband. Previous research has shown that aggregates generally produce lower values of K_{DP} than dry crystals (Ryzhkov and Zrnich 1998; Straka et al. 2000; May and Keenan 2005). It is possible that the aggregates in this study had a more horizontal orientation similar to the large, low density aggregates sampled by Meischner et al. (1991).

Average DOW ρ_{HV} values both inside (0.97) and outside (0.96) the snowband are consistent with ρ_{HV} values for aggregates from Straka et al. (2000) and May and Keenan (2005). For the UND radar, the average ρ_{HV} value inside the snowband is 0.93, while the average value outside 0.85. The inside UND average ρ_{HV} value is very close to the ρ_{HV} value for aggregates from Straka et al. (2000) and May and Keenan (2005), while the outside UND average ρ_{HV} value is more consistent with the ρ_{HV} value for wet snow from Straka et al. (2000), May and Keenan (2005), and Ahasic et al. (2012). Possible reasons for the differences between the DOW and UND polarimetric values are differences in radar calibration and sensitivity, noise in the UND polarimetric data, slight differences in the area of the snowband sampled by each radar, and small-scale variations within the snowband.

Plummer et al. (2014) analyzed the microphysical structure of stratiform precipitation in the comma head of multiple continental cyclones, and found a greater concentration of larger hydrometeors inside generating cells². Additional findings by Plummer et al. (2014) were larger hydrometeors, higher LWC, and SLW were also present within the sampled generating cells, indicating that generating cells were likely favorable regions for ice growth. Since snowbands can occur in the northwest quadrant of extratropical cyclones (Cronce et al. 2007; Novak et al. 2009) and the snowband in this study had greater concentrations of larger

² A generating cell is a small region of locally high reflectivity from which a trail of hydrometeors originates.

hydrometeors inside versus outside, the ice growth processes of generating cells from Plummer et al. (2014) could be relevant to this study.

Project Limitations

Aircraft and radar data are affected by various limitations. For the aircraft, the only hydrometeor sampling instrument available at the time of the experiment was the 2DC probe, which is designed to measure hydrometeors between 30 – 3000 μm . The actual size of all precipitation-sized hydrometeors larger than which can be measured with the 2DC is unknown. Second, winds within a snowband might be so weak that vertical velocity measurements from the aircraft are close to the instrument noise level. Previous studies of individual generating cells indicate that vertical velocity within the center of the cells was $\pm 1 - 2 \text{ m s}^{-1}$ (Rosenow et al. 2014) while the relative uncertainty of the vertical wind speed from the air speed measurement system on the aircraft is 0.1 m s^{-1} (Delene 2015). Lastly, aircraft data inside and outside the snowband were only collected at lower altitudes (below 2.71 km), whereas the snowband extended to altitudes up to 9 km AGL. Radar cross sections of dual-Doppler retrieved values of vertical velocity show the strongest values located 4 – 6 km AGL – above the aircraft sample altitudes.

Another aircraft limitation was the small sampling area of the aircraft relative to the entire snowband size, both horizontally and vertically. The strongest areas of vertical velocity as indicated by the retrieved dual-Doppler analysis were not sampled by the aircraft. The aircraft did not fly at a high enough altitude and the area sampled seemed to be the transition between the strongest upward and downward motion areas.

Another limitation is the analysis of the winds using dual-Doppler wind retrieval.

Although radar data were collected with the WSR-88D S-band radar KMVX stationed near Mayville, ND, triple-Doppler analysis were not utilized owing to artifacts present within them. Radar rings described in **Artifacts Arising from Multi-Doppler Objective Analysis Process** were present with KMVX data as well. The same smoothing technique applied to DOW and UND data to smooth the rings was also applied to early results using KMVX data. However, triple-Doppler analysis created unrealistic positive and negative vertical velocity artifacts along the aircraft transect. Dual-Doppler analyses for each of the three radar pairs (DOW-KMVX, UND-KMVX, DOW-UND) does not have the positive and negative vertical velocity artifacts along the transect. The unrealistic vertical velocity artifacts in the triple-Doppler data were caused by transition from triple-Doppler to dual-Doppler analysis. Since velocity data from only the DOW and UND radars are used, the parametric system of equations is underdetermined (four unknowns with only two parametric equations and one terminal fallspeed equation). Using a third radar would provided a radar measurement for the wind field component w , as opposed to using the anelastic mass continuity equation, used for dual-Doppler analysis, to estimate the value for w . In addition, the dual Doppler coverage area is not large enough to encompass the entire snowband, which limits the analysis region wherein perpendicular cross sections could be analyzed. Lastly, the power-weighted mean precipitation terminal fall speeds could only be estimated from the radar reflectivity values as actual snow fall speeds were not collected during the study. The truncated size distribution from the 2DC probe does not enable estimation of power-weighted terminal fallspeed either. This property is needed in (13) to obtain the most accurate wind-field estimation possible.

Finally, data from **Aircraft Results** shows that particle concentrations and diameters gradually change both inside and outside the snowband with changing altitudes. Another

project limitation is that the exact cause of the concentration/diameter change with altitude is still unknown. This change could be a result of changing altitudes, temporal evolution, or both. Because the aircraft was only flown at lower altitudes, the sampled hydrometeors may represent characteristics later in their growth history. Fall streaks studied by Plummer et al. (2015) have similar hydrometeor concentration distributions as snowbands. Since generating cells and fall streaks have similar characteristics as snowbands, the hydrometeor characteristics and environmental conditions in fall streaks studied by Plummer et al. (2015) could be used to speculate what conditions influence hydrometeor growth within different vertical levels of a snowband.

CHAPTER V

CONCLUSIONS

In this study, the 20-21 November 2010 airflow and hydrometeor characteristics within a Meso- γ snowband, embedded within a larger area of snow, are studied. Snowbands are known to cause low-visibility conditions, a hazardous situation for ground and air transportation. The snow size distributions measured *in situ* with aircraft instrumentation are related to the remotely-sensed dual-polarimetric radar variables. These hydrometeor distributions are then related to the airflow patterns, which are retrieved using dual-Doppler wind retrieval.

In this study, analysis of the 2DC probe images shows a greater concentration of larger hydrometeors inside a snowband, while a greater concentration of smaller hydrometeors is present outside the snowband. Concentrations of larger hydrometeors inside (outside) the snowband decrease (increase) with decreasing altitude. The differences in concentration and size are more noticeable at higher altitudes than at lower altitudes. Greater concentrations of larger hydrometeors at the highest sampled altitude inside the snowband would provide continued evidence that upward motion is present within snowbands. Previous research has found greater precipitation intensity within winter storm updrafts rather than downdrafts, suggesting larger ice crystals and faster snow growth within updrafts (Coronce et al 2007).

By definition, both UND and DOW reflectivities are greater inside the snowband. For both radars, inside the snowband average K_{DP} values are larger for most altitudes, and average ρ_{HV} values are larger for all five altitudes. Average DOW Z_{DR} values are closer to 0 dB inside the snowband. However the UND radar Z_{DR} values are closer to 0 dB outside the snowband. Snowband propagation, radar calibration differences, and noise in the radar data are thought to be the possible reasons for different Z_{DR} pattern observed with the UND radar. Previous studies of different snow environments show that reflectivity is greater and Z_{DR} is closer to 0 dB for aggregated hydrometeors (Meischner et al. 1991; Straka et al. 2000; May and Keenan 2005), K_{DP} is lower for aggregates than dry crystals (Ryzhkov and Zrnich 1998; Straka et al. 2000; May and Keenan 2005), and ρ_{HV} values above 0.95 indicate aggregates (Straka et al. 2000; May and Keenan 2005).

No significant differences in the retrieved velocity pattern along the first and second transect-pairs are present inside compared to outside the snowband. For the third and fourth transect-pairs, inside the snowband has predominantly downward motion (not accounting for radar/aircraft bias) while the outside transects have both upward and downward motion. For the fifth transect-pair, both inside and outside have predominantly upward motion along both transects, however the area of upward motion is larger in the outside transect. The dual-Doppler-retrieved horizontal flow both inside and outside the snowband changes from easterly at lower altitudes to westerly at higher altitudes. This direction shift was consistent with winds observed with the nearest sounding (Bismarck, ND). Aircraft-measured averaged temperature and vertical velocities at each altitude do not differ significantly inside versus outside the snowband.

When examining the entire analysis region, vertical velocity direction (up/down) is different for the opposing analysis lobes with the switch occurring near the DOW radar location. Upward motion is seen generally west of the DOW location, with downward motion generally around and to the east. Although the upward/downward switch is near the DOW radar in the DOW/UND retrieval case, other radar pairs (DOW/KMVX, UND/KMVX) had similar upward/downward motions around the same general region. Thus the DOW/UND upward/downward switch coinciding near the DOW location is not believed to be a radar or analysis artifact.

Level aircraft transects through a snowband are divided up into transects through the snowband edge and core. This allows aircraft and radar comparisons of different snowband sections that are much closer in time. The vertical velocity values in the snowband edge and core are the same, which is not consistent with the original hypothesis. Average Z_{DR} values in the snowband edge are greater than those in the core for both cases. This indicates hydrometeors with a more circular orientation within the core, which is consistent with the original hypothesis.

From the original hypothesis: stronger reflectivity and Z_{DR} values closer to 0 dB inside the snowbands should coincide with stronger updrafts within the snowband. From the results, radar reflectivity values inside the snowband core are both greater than those outside the snowband core (part of snowband definition) as well as possessing Z_{DR} values closer to 0 dB inside the snowband. However areas of stronger reflectivity and Z_{DR} values closer to 0 dB do not coincide with stronger updrafts inside the snowband. The vertical velocity measured by the aircraft as well as the vertical velocity retrieved from dual-Doppler analysis has similar values both inside and outside the snowband. Using the results from this study, a

revised hypothesis is: stronger reflectivity and Z_{DR} values closer to 0 dB inside the snowbands coincide with snow aggregates, however these aggregates do not always coincide with stronger updrafts within the snowband.

As mentioned at the beginning of Chapter I, predicting snowband location and intensity continue to prove challenging for forecasting models. Accurate snowband predictability is related to the quality of the initial conditions, and use of forecasting model grids small enough to resolve mesoscale features (Novak and Colle 2012). Results from the current study and earlier analysis of the same dataset (Robak et al. 2012) illustrate that polarimetric and size distribution characteristics of snow differ in and out of snowbands. While differences in reflectivity are evident inside and outside the snowband, retrieved vertical velocity do not differ significantly inside versus outside the snowband. Results from this and further studies could be used to verify (and thus potentially improve the microphysics parameterization within) forecasting models of cold season events. Accurately forecasting the timing, duration, and snowfall amounts from snowbands could be used to improve transportation safety and efficiency.

Although more accurate Doppler wind retrievals are theoretically possible using three Doppler radars, doing so using CEDRIC can result in corrupted or reduced accuracy in needed portions of the analysis space (see **Project Limitations**). Because the small-scale snowband is larger than the triple-Doppler analysis region, some portions of the snowband have corrupted winds when using triple-Doppler analyses (particularly directly over the radar site). Corrupt winds using triple-Doppler analysis is why dual-Doppler analysis was used.

To improve upon this study, additional types of data could be collected and utilized. Measurements of precipitation terminal fall speed either from a vertically-pointing radar or

estimated using an aircraft precipitation probe such as the High Volume Precipitation Spectrometer probe (HVPS) could provide more accurate measurements of the hydrometeor terminal velocity, for that case. Instead of estimating the precipitation terminal fall speed, actual measurements would improve the multi-Doppler wind retrieval. Accurate measurements of the hydrometeor terminal velocity could be used to bias-correct the dual-Doppler wind retrieval. Aircraft instruments for collecting data regarding the full size spectrum of precipitation-size hydrometeors, such as the HVPS, could also be used to greatly improve knowledge regarding the larger sized snowflakes within the snow size distribution. Snowfall and visibility measurements both inside and outside the snowband could also be used to better quantify snowband impacts near ground level. Finally, data from this and other experiments could be used to improve the snow microphysical parameterizations, which should improve the forecast models.

APPENDICES

Appendix A

2-D Optical Array Probe Particle Reconstruction Method

The 2-D Optical Array Probe is designed to measure cloud droplets and cannot measure hydrometeors larger than 3000 μm (Particle Measuring Systems, Inc.). Recorded hydrometeors by the 2DC probe that have only a portion of their shape visible or are larger than the max observing size are reconstructed to determine the approximate two-dimensional hydrometeor size and shape. For this reconstruction to be possible the ratio of the portion y axis to the portion x axis must be at least 0.2. Simply removing hydrometeors only partially visible from the sampled volume would reduce the efficiency of the probe, however including only the visible portion of the hydrometeor in the sample area would underestimate particle dimension and sampling volume (Heymnsfield and Parrish 1978).

If the sampled hydrometeor only has one side obscured (Fig. 31a) then the hydrometeor size can be calculated from

$$D = \frac{\left(\frac{x_1}{2}\right)^2 + y_1^2}{y_1}, \quad (18)$$

where x_1 and y_1 are the axis dimensions of the hydrometeor portion within the sampling area and D is the calculated hydrometeor size. For hydrometeors larger than the max observing size (Fig. 31b) the calculation is

$$D = \left[\left(y_1 + \frac{x_2^2 - x_1^2}{4y_1} \right)^2 + x_1^2 \right]^{\frac{1}{2}}. \quad (19)$$

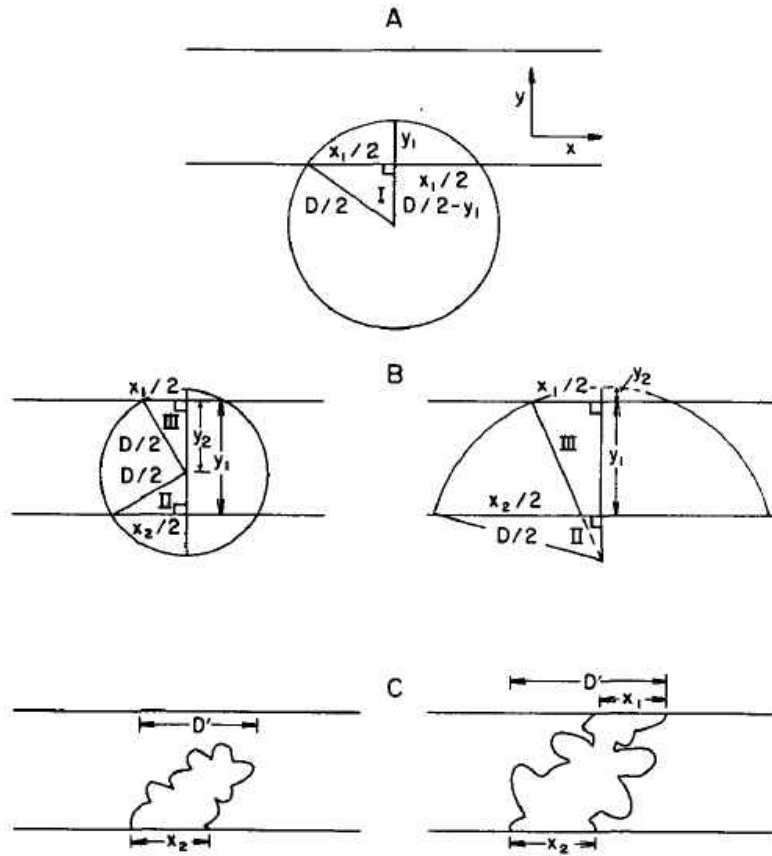


Fig. 31. Geometry used to recompute diameter of hydrometeors: (a) circular hydrometeor obscuring one end; (b) circular hydrometeor obscuring two ends, with hydrometeor center inside of sensing area (left) and outside of sensing area (right); and (c) aggregate of hydrometeors touching one end of sensing area (left) and touching both ends of sensing area (right). Adapted from Heymsfield and Parrish (1978).

Appendix B

Location of Data and Programs

The data and programs used in this study are located on University of North Dakota Department of Atmospheric Science computer storage and storage with the author's personal computer. Radar data, radar processing program, multi-Doppler retrieval and display programs, aircraft data, and aircraft processing program are located on the Department of Atmospheric Science computer 'radar2' under the /data2 directory. Processed plots are located under the author's home directory on the UND Aerospace computer network. The final plots, aircraft-to-radar conversion programs, and written documents are located on the author's personal computer.

REFERENCES CITED

- Ahasic, E. T., J. W. Frame, and T. R. Cermak, 2012: Classification of precipitation types in lake-effect snow events using dual-polarimetric Doppler radar observations. Preprints, *16th Symp. on Meteorological Observation and Instrumentation*, New Orleans, LA, Amer. Meteor. Soc., P6.4.
- Armijo, L., 1969: A theory for the determination of wind and precipitation velocities with Doppler radars. *J. Atmos. Sci.*, **26**, 570–573.
- Askelson, M., Jean-Pierre. Aubagnac, and J. M. Straka, 2000: An adaptation of the Barnes filter applied to the objective analysis of radar data. *Mon. Wea. Rev.*, **128**, 3050–3082.
- Atlas, D., R. C. Srivastava, and R. S. Sekhon, 1973: Doppler radar characteristics of precipitation at vertical incidence. *Rev. Geophys. Space Phys.*, **11**, 1-35.
- Aubagnac, Jean-Pierre., M. Askelson, B. Gordon, A. Theisen, K. LaRoche, 2013: Cutsome.
- Aydin, K., V. N. Bringi, and L. Liu, 1995: Rain-rate estimation in the presence of hail using S-band specific differential phase and other radar parameters. *J. Appl. Meteor.*, **34**, 404–410.
- Brandes, E. A., J. Vivekanandan, J. D. Tuttle, and C. J. Kessinger, 1995: A study of thunderstorm microphysics with multiparameter radar and aircraft observations. *Mon. Wea. Rev.*, **123**, 3129–3143.
- Brandes, E. A., 2000: Dual-polarization radar fundamentals and algorithm prospects. 8 pp. <http://www.roc.noaa.gov/wsr88d/PublicDocs/AppsDocs/algorithm00.pdf>.
- Center for Severe Weather Research, 2015: DOW 6 Specs. Accessed May 2015. [Available online at <http://www.cswr.org/contents/dow7specs.php>]
- Cermak, T. R., J. W. Frame, and E. T. Ahasic, 2012: Dual-polarization observations of vortices and cellular convection within lake-effect snow bands. Preprints, *16th Symp. on Meteorological Observation and Instrumentation*, New Orleans, LA, Amer. Meteor. Soc., P6.6.
- Cressman, G. P., 1959: An operational objective analysis system. *Mon. Wea. Rev.*, **87**, 367–374.

- Cronce, M., R. M. Rauber, K. R. Knupp, B. F. Jewett, J. T. Walters, and D. Phillips, 2007: Vertical motions in precipitation bands in three winter cyclones. *J. Appl. Meteor. Climatol.*, **46**, 1523–1543.
- Delene, D. J., et al. (2015), Airborne Data Processing and Analysis (Revision Version 2000), Source Forge, URL: <http://sourceforge.net/projects/adpaa/>, Retrieved January 18, 2015, DOI: 10.5281/zenodo.14053.
- Delene, D. J., cited 2015, University of North Dakota's Citation Aircraft Winds Calculation. Department of Atmospheric Science. University of North Dakota. [Available online at <http://aerosol.atmos.und.edu/ADPAA/winds/index.html>.]
- Dixon, M., 2010: Radx C++ Software Package for Radial Radar Data. National Center for Atmospheric Research.
- Dixon, M., and J.C. Hubbert, 2012: The separation of noise and signal components in Doppler RADAR returns. *7th European Conference on Radar in Meteorology and Hydrology*, Toulouse, France.
- Glickman, T. S., 2000: *American Meteorological Society Glossary of Meteorology*. 2nd ed. American Meteorological Society.
- Heymsfield, A. J., and J. L. Parrish, 1978: A computational technique for increasing the effective sampling volume of the PMS two-dimensional Particle Size Spectrometer. *J. Appl. Meteor.*, **17**, 1566–1572.
- Hogan, R. J., P. R. Field, A. J. Illingworth, R. J. Cotton, and T. W. Choullarton, 2002: Properties of embedded convection in warm-frontal mixed-phase cloud from aircraft and polarimetric radar. *Quart. J. Roy. Meteor. Soc.*, **128**, 451–476.
- Houser, J., and H. B. Bluestein, 2011: Polarimetric Doppler radar observations of Kelvin–Helmholtz waves in a winter storm. *J. Atmos. Sci.*, **68**, 1676–1702.
- Ikeda, K., and E. A. Brandes, 2003: Freezing level determinations with polarimetric radar: Retrieval model and application. Preprints, *31st Int. Conf. on Radar Meteorology*, Seattle, WA, Amer. Meteor. Soc., 649–652.
- Joss, J., and A. Waldvogel, 1970: A method to improve the accuracy of radar measured amounts of precipitation. Preprints, *14th Radar Meteorology Conf.*, Tucson, AZ, Amer. Meteor. Soc., 237–238.
- Kawashima, M., and Y. Fujiyoshi, 2005: Shear instability wave along a snowband: Instability structure, evolution, and energetics derived from Dual-Doppler radar data. *J. Atmos. Sci.*, **62**, 351–370.

- Kennedy, P. C., and S. A. Rutledge, 2011: S-band dual-polarization radar observations of winter storms. *J. Appl. Meteor. Climatol.*, **50**, 844–858.
- Kocin, P. J., and L. W. Uccellini, 2004: Mesoscale aspects of northeast snowfall distribution. *Northeast Snowstorms*. Vol 1. Meteor. Monogr., No. 54, Amer. Meteor. Soc., 177–206.
- Lenschow, D. H., 1986: Aircraft measurements in the boundary layer. *Probing the Atmospheric Boundary Layer*, D. H. Lenschow, Ed., Amer. Meteor. Soc., 39–55.
- May, P. T., and T. D. Keenan, 2005: Evaluation of microphysical retrievals from polarimetric radar with wind profiler data. *J. Appl. Meteor.*, **44**, 827–838.
- Meischner, P., V. N. Bringi, M. Hagen, and H. Holler, 1991: Multiparameter radar characterization of a melting layer compared with *in situ* measurements. Preprints, *25th Int. Conf. on Radar Meteorology*, Paris, France, Amer. Meteor. Soc., 721–724.
- Merritt, J. H., and D. B. Wolff, 2015: The Radar Software Library. Version 1.25 NASA/TRMM Office. [Available online at http://trmm-fc.gsfc.nasa.gov/trmm_gv/software/rsl/]
- Miller, L. J., and S. M. Fredrick, 2009: CEDRIC Custom Editing and Display of Reduced Information in Cartesian space. National Center for Atmospheric Research, Mesoscale and Microscale Meteorology Division.
- National Center for Atmospheric Research – Atmospheric Technology Division. 2009: SOLO, Software for the analysis of airborne, WSR-88D, and other radar data, (NCAR/ATD) Edition 2.2. NCAR/ATD
- Nissen, R., D. Hudak, S. Laroche, R. Elía, I. Zawadzki, and Y. Asuma, 2001: 3D wind field retrieval applied to snow events using Doppler radar. *J. Atmos. Oceanic Technol.*, **18**, 348–362.
- Novak, D. R., L. F. Bosart, D. Keyser, and J. S. Waldstreicher, 2004: An observational study of cold season–banded precipitation in northeast U.S. cyclones. *Wea. Forecasting*, **19**, 993–1010.
- Novak, D. R., B. A. Colle, and R. McTaggart-Cowan, 2009: The role of moist processes in the formation and evolution of mesoscale snowbands within the comma head of northeast U.S. cyclones. *Mon. Wea. Rev.*, **137**, 2662–2686.
- Novak, D. R., and B. A. Colle, 2012: Diagnosing snowband predictability using a multimodel ensemble system. *Wea. Forecasting*, **27**, 565–585.

- Oye, D., and M. Case, 1995: REORDER: A program for gridding radar data – Installation and use manual for the UNIX version. Atmospheric Technology Division, National Center for Atmospheric Research, 14-18 pp. [Available from Atmospheric Technology Division, NCAR, P.O. Box 3000, Boulder, CO 80307.]
- Particle Measuring Systems, Inc.: 2015. SN: 685-0478-07. 2-D Optical Array Spectrometer Probe PMS Model OAP-2D-C Serial No. 685-0478-07 Operating Manual.
- Pierce, D. W. 2003: Ncview software, Edition 1.92e.
- Plummer, D. M., G. McFarquhar, R. Rauber, B. Jewett, and D. Leon, 2014: Structure and statistical analysis of the microphysical properties of generating cells in the comma head region of continental winter cyclones. *J. Atmos. Sci.*, **71**, 4181–4203.
- Plummer, D. M., G. McFarquhar, R. Rauber, B. Jewett, and D. Leon, 2015: Microphysical properties of convectively generated fall streaks within the stratiform comma head region of continental winter cyclones. *J. Atmos. Sci.*, **72**, 2465–2483.
- Plymouth State Weather Center, 2015: Make Your Own... Product Generator for Archived Data. [Available online at <http://vortex.plymouth.edu/u-make.html>]
- Rasmussen, R. M., A. Crook, and C. Kessinger, 1993: Snow-band formation and evolution during the 15 November 1987 aircraft accident at Denver Airport. *Wea. Forecasting*, **8**, 453–480.
- Rauber, R. M., and A. Tokay, 1991: An explanation for the existence of supercooled water at the top of cold clouds. *J. Atmos. Sci.*, **48**, 1005–1023.
- Ray, P. S., C. L. Ziegler, W. Bumgarner, and R. J. Serafin, 1980: Single- and multiple-Doppler radar observations of tornadic storms. *Mon. Wea. Rev.*, **108**, 1607–1625.
- Rinehart, R. E., 2010: *RADAR for Meteorologists*. 5th ed. Rinehart Publications.
- Robak, H., M. Gilmore, M. Askelson, C. Theisen, and D. Delene, 2012: Hydrometeor classification of snow using a fuzzy logic method. Poster. 12th Annual AMS Student Conference, Austin, TX.
- Rosenow, A. A., D. Plummer, R. Rauber, G. McFarquhar, B. Jewett, and D. Leon, 2014: Vertical velocity and physical structure of generating cells and convection in the comma head region of continental winter cyclones. *J. Atmos. Sci.*, **71**, 1538–1558.
- Ryzhkov, A. V., and D. S. Zrnic, 1998a: Discrimination between rain and snow with a polarimetric radar. *J. Appl. Meteor.*, **37**, 1228–1240.
- Ryzhkov, A. V., T. J. Schuur, D. W. Burgess, and D. S. Zrnic, 2005: Polarimetric tornado detection. *J. Appl. Meteor.*, **44**, 557–570.

- Satoh, S., and J. Wurman, 2003: Accuracy of wind fields observed by a bistatic Doppler radar network. *J. Atmos. Oceanic Technol.*, **20**, 1077–1091.
- Scharfenberg, K. A., and E. Maxwell, 2003: Operational use of a hydrometeor classification algorithm to detect the snow melting level. Preprints, *31st Int. Conf. on Radar Meteorology*, Seattle, WA, Amer. Meteor. Soc., 639–641.
- Schultz, D. M., and P. N. Schumacher, 1999: The use and misuse of conditional symmetric instability. *Mon. Wea. Rev.*, **127**, 2709–2732.
- Shapiro, A., K. M. Willingham, and C. K. Potvin, 2010: Spatially variable advection correction of radar data. Part II: Test results. *J. Atmos. Sci.*, **67**, 3457–3470.
- Steiger, S. M., R. Schrom, A. Stamm, D. Ruth, K. Jaszka, T. Kress, B. Rathbun, J. Frame, J. Wurman, and K. Kosiba, 2013: Circulations, bounded weak echo regions, and horizontal vortices observed within long-lake-axis-parallel-lake-effect storms by the Doppler on Wheels. *Mon. Wea. Rev.*, **141**, 2821–2840.
- Straka, J. M., D. S. Zrnić, and A. V. Ryzhkov, 2000: Bulk hydrometeor classification and quantification using polarimetric radar data: Synthesis of Relations. *J. Appl. Meteor.*, **39**, 1341–1372.
- Thunis, P., and R. Bornstein, 1996: Hierarchy of mesoscale flow assumptions and equations. *J. Atmos. Sci.*, **53**, 380–397.
- University of North Dakota, 2004: UND Polarimetric Doppler Radar. Department of Atmospheric Sciences. Accessed May 2015. [Available online at <http://radar.atmos.und.edu/layout.php?page=specs>]
- Wang, Y., and V. Chandrasekar, 2009: Algorithm for estimation of the specific differential phase. *J. Atmos. Oceanic Technol.*, **26**, 2565–2578.
- Wolde, M., and G. Vali, 2001: Polarimetric signatures from ice crystals observed at 95 GHz in winter clouds. Part I: Dependence on crystal form. *J. Atmos. Sci.*, **58**, 828–841.
- Zrnić, D. S., and A. V. Ryzhkov, 1999: Polarimetry for weather surveillance radars. *Bull. Amer. Meteor. Soc.*, **80**, 389–406.
- Zrnić, D. S., A. V. Ryzhkov J., Straka, Y. Liu, and J. Vivekanandan, 2001: Testing a procedure for automatic classification of hydrometeor types. *J. Atmos. Oceanic Technol.*, **18**, 892–913.